Flexibility of Duplex DNA on the Submicrosecond Timescale

T. M. Okonogi*, A. W. Reese*, S. C. Alley*,#, P. B. Hopkins*, and B. H. Robinson*
*Department of Chemistry, University of Washington, Seattle, Washington 98195-1700, and #Department of Chemistry, The Pennsylvania State University, University Park, Pennsylvania 16802

ABSTRACT Using a site-specific, Electron Paramagnetic Resonance (EPR)-active spin probe that is more rigidly locked to the DNA than any previously reported, the internal dynamics of duplex DNAs in solution were studied. EPR spectra of linear duplex DNAs containing 14–100 base pairs were acquired and simulated by the stochastic Liouville equation for anisotropic rotational diffusion using the diffusion tensor for a right circular cylinder. Internal motions have previously been assumed to be on a rapid enough time scale that they caused an averaging of the spin interactions. This assumption, however, was found to be inconsistent with the experimental data. The weakly bending rod model is modified to take into account the finite relaxation times of the internal modes and applied to analyze the EPR spectra. With this modification, the dependence of the oscillation amplitude of the probe on position along the DNA was in good agreement with the predictions of the weakly bending rod theory. From the length and position dependence of the internal flexibility of the DNA, a submicrosecond dynamic bending persistence length of around 1500 to 1700 Å was found. Schellman and Harvey (Biophys. Chem. 55:95–114, 1995) have estimated that, out of the total persistence length of duplex DNA, believed to be about 500 Å, approximately 1500 Å is accounted for by static bends and 750 Å by fluctuating bends. A measured dynamic persistence length of around 1500 Å leads to the suggestion that there are additional conformations of the DNA that relax on a longer time scale than that accessible by linear CW-EPR. These measurements are the first direct determination of the dynamic flexibility of duplex DNA in 0.1 M salt.

INTRODUCTION

The nature of the flexibility of individual base pairs in duplex DNA has been an ongoing concern of biophysical research. The fundamental question is: "whether simple coupled Langevin equations and generalized diffusion equations for such motions are valid at nanosecond times, in the presence of strong direct forces." (Schurr et al., 1992). The theory of deformability of an elastic filament in a simple solvent with normal viscosity is well developed, easy to implement, and test by experiment (Song et al., 1990; Wu et al., 1987). This theory of the dynamics, when applied to duplex DNA, is capable of predicting both the mean square amplitudes of twisting and bending oscillations of base pairs within the duplex DNA as well as the decay times of each of the normal modes of deformation.

The dynamics of DNA have been studied by such techniques as time-resolved fluorescence polarization anisotropy (Barkley and Zimm, 1979; Schurr et al., 1992), transient photodichroism (Allison et al., 1989), and electric birefringence (Hagerman, 1988). In all cases, because the probes were uniformly distributed along the length of the DNA, the measured dynamic responses of the system were averaged over the entire DNA. To test theories of the elastic properties of duplex DNA as a function of local sequence and local position requires probes that can be placed unambiguously at specific sites along the DNA. Much work has been done to develop such probes for electron paramagnetic resonance (EPR) and nuclear magnetic resonance (NMR) (Alam and Drobny, 1991; Eimer et al., 1990; Robinson and Drobny, 1995b; Robinson et al., 1997). NMR experiments generally use spin-active nuclear isotopes, such as deuterium (Mattiello and Drobny, 1994; Nuutero et al., 1994). Drobny has noted individual librational dynamics of sugars that are site and sequence dependent (Robinson et al., 1997).

The model-free approach to analyzing EPR (Keyes and Bobst, 1995; Strobel et al., 1995; Thomas et al., 1975) and NMR (Lipari and Szabo, 1981, 1982a,b; Robinson and Drobny, 1995a) data to extract dynamics information has been heavily used in the last few years. The goal of the model-free approach is to determine the order parameters (or mean square amplitudes of motion) and internal correlation times from experimental line width data. However, for the EPR data presented herein, there exist no well developed methods for extracting a dynamics-sensitive line width, and therefore the traditional model-free approach is inappropriate. Nevertheless, the analysis used does yield the order parameters associated with the internal dynamics via the mean square amplitude parameters, which are completely equivalent to the order parameters, S_i, obtained by a model-free approach (Schurr et al., 1994). More importantly, the dynamics model of choice, which is the weakly bending rod model, predicts the dependence of the order parameters on label position in the sequence and the length of the DNA.

Site-specific probes allow one to test predictions of changes in DNA motion as a function of position and sequence. Spectra are sensitive to the mean square oscillation amplitudes and the decay times of the modes of motion. Some analyses have alluded to the existence of large (>25°)

Received for publication 24 June 1999 and in final form 24 August 1999.
Address reprint requests to Dr. Bruce H. Robinson, Department of Chemistry, University of Washington, Box 351700, Seattle, WA 98195. Tel.: 206-543-1773; Fax: 206-685-8665; E-Mail: robinson@chem.washington.edu.

0006-3495/99/12/3256/21 $2.00

amplitudes of motion of base pairs (Hogan and Jardetzky, 1979, 1980; Keyes and Bobst, 1995; Strobel et al., 1995). A careful reanalysis of much of these data has indicated that the apparently large amplitudes can be explained by a superposition of collective deformations and local motions at the base pair level that are individually of smaller amplitude. For example, Eimer et al. (1990) found the amplitude of motion to be ~18° and was cited (Keyes and Bobst, 1995) as a demonstration that base pairs of DNA have large amplitudes of local motion, but when the data were reanalyzed by Nuutero et al. (1994), using a collective modes model, the residual amplitudes of local motion were less than 10°.

EPR labeling experiments have focused on replacing natural bases with analogs modified to contain the EPR active nitroxide radical as an integral part of the base. Early site-specific probes underwent substantial probe motion with order parameters less than 0.4 (Keyes and Bobst, 1995; Strobel et al., 1995). Later developments generated a class of probes with order parameters of 0.5 and 0.8 (Hustedt et al., 1993a, 1995). Recently, a new EPR-active spin-probe, *Q*, that has an order parameter greater than 0.95 (Miller et al., 1995), has been synthesized, and we report here the results obtained by using it. Such a probe can be expected to have greater sensitivity to the collective modes that characterize the internal deformations of the DNA (Robinson and Drobny, 1995a; Robinson et al., 1997) and be sensitive to dynamic processes with correlation times as long as one microsecond (Freed, 1976; Hustedt et al., 1993a). Magnetic resonance experiments uniquely distinguish among 1) rapid internal relaxation when the decay times are faster than one nanosecond, 2) the decay times for internal dynamics themselves when those decay times are on the order of nanoseconds, and 3) the uniform modes, whose reorientation times may be microseconds or longer.

The weakly bending rod model of DNA dynamics relates the mean square amplitudes of oscillation to the force constant for bending between base pairs, which, in turn, is simply related to the dynamic-flexural persistence length. The total duplex DNA persistence length is nominally around 500 Å, and contains both dynamic and static components. Trifonov et al. (1987) suggested that the total persistence length, P_t, be written as the sum of a dynamic component, P_d, and a static (structural) component, P_s: $1/P_t = 1/P_s + 1/P_d$. Schellman and Harvey (1995) have confirmed the Trifonov relation. The Schellman–Harvey estimate for P_s is sequence dependent and ranges from $P_s \sim$ 1370 Å for a "many wedge model" to $P_s \sim 2000$ Å for the AA-wedge model. To date, there have been no direct measurements on the dynamic component of DNA when not subjected to an external-distorting field. In the following experiments, we provide direct evidence for the dynamic component of the persistence length. We note that the EPR experiments are sensitive to dynamics on the submicrosecond time scale; therefore, our EPR measurements are not sensitive to dynamics longer than a microsecond. The relaxation observed in these experiments could be considered to be fast dynamics due to bending (db), and the associated persistence length is called, P_{db}. There potentially are slowly relaxing structures (srs) that relax on a timescale slower than our experiment can observe. The overall dynamic persistence length would then be the sum in the same form as above: $1/P_d = 1/P_{srs} + 1/P_{db}$. Substituting this relation into the above expression, we suggest that the total persistence length is the sum of three components (Schurr et al., 1997): $1/P_t = 1/P_s + 1/P_{db} + 1/P_{srs}$.

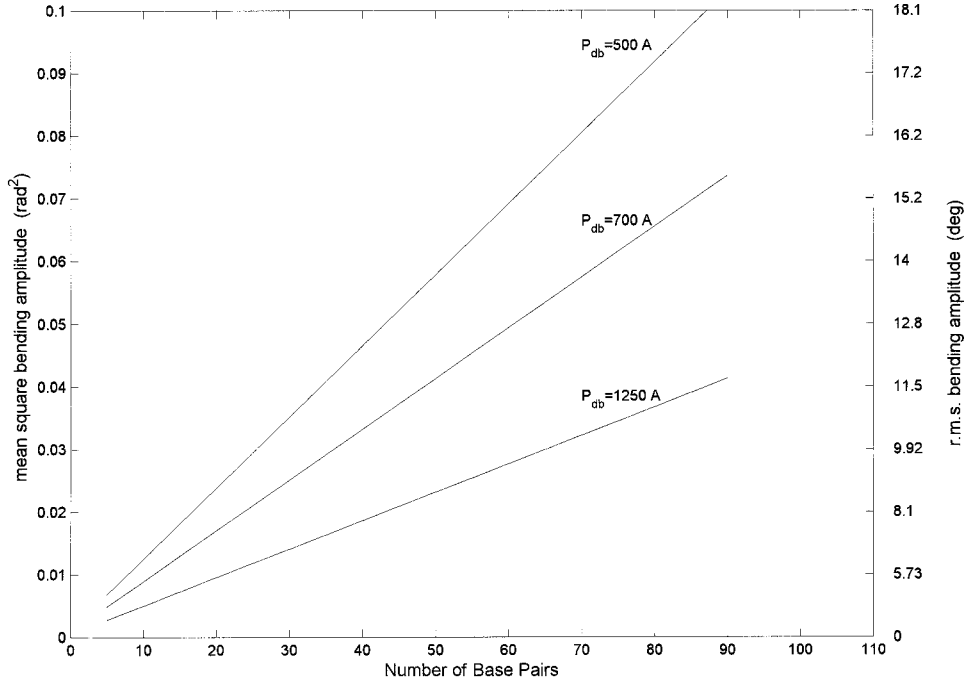

FIGURE 1 Plot of $2\langle\eta_i^2\rangle$ for three different persistence lengths—500, 700, and 1250 Å—as computed by Eq. 3. The left-hand *y*-axis are the mean square amplitudes in rad^2 for $i = (N + 1)/2$ (middle-label) DNA versus $(N + 1)$ base pairs, and the right-hand *y*-axis the corresponding r.m.s. angular displacements of bending in both directions, in degrees.

Figure 1 illustrates the dependence of the mean square bending oscillation amplitude (in rad^2), and the root mean square angular displacement (in degrees), for the central base ($i = (N + 1)/2$) of the weakly bending rod model as a function of the number of base pairs, $N + 1$, of DNA for various values of the dynamic persistence length. As shown, the mean square oscillation amplitude is sensitive to the dynamic persistence length, easily distinguishing between 500-, 750-, and 1250-Å persistence lengths. In this paper, we will measure P_{db} using the weakly bending rod model and demonstrate that the weakly bending rod model is valid for the dynamics as a function of DNA length and probe position on the DNA.

APPLICATION OF THE THEORY OF THE WEAKLY BENDING ROD TO EPR SPECTRA

We summarize the simple and elegant weakly bending rod model developed by Schurr and coworkers (Schurr et al., 1992; Song et al., 1990; Wu et al., 1987) to describe the modes of motion of DNA. Mathematically, DNA is treated as a flexible rod-shaped object. Although duplex DNA may be curved over a long distance, mean local cylindrical symmetry is assumed to occur about each base, and each base is attached to neighboring bases by a Hookean spring. The model predicts the mean-square amplitudes of both twisting $\langle \phi_i^2 \rangle$ and bending $\langle \eta_i^2 \rangle$ of the ith base pair in a duplex DNA consisting of $N + 1$ base pairs.

The total twisting potential energy is $U = \frac{1}{2}\alpha \vec{\phi}^t A \vec{\phi}$, where α is the twisting force constant, $\vec{\phi}$ is a column vector of $N + 1$ twisting angles with $\vec{\phi}^t$ its transpose, and $\mathbf{A}$ is the $N + 1$ by $N + 1$ harmonic coupling matrix, given in Eq. A3. In terms of the normal modes of motion,

$$\langle \vec{\phi}(\infty)\vec{\phi}^t(\infty)\rangle = \int_{-\infty}^{\infty} \vec{\phi} P(\phi) \vec{\phi}^t \, d\phi^N$$

$$= Q \int_{-\infty}^{\infty} \vec{\rho} \frac{\exp\{-U/k_BT\}}{\int \exp\{-U/k_BT\}\, d\rho^N} \vec{\rho}^t \, d\rho^N Q^t$$

$$= \frac{k_BT}{\alpha} Q\Lambda^{-1}Q^t, \tag{1a}$$

where $P(\phi)$ is the Boltzmann probability distribution. $\mathbf{Q}$ is the real, orthogonal transformation matrix that diagonalizes $\mathbf{A}$, where $\mathbf{Q}^t\mathbf{Q} = 1$. $\mathbf{\Lambda}$ is the diagonal matrix of eigenvalues of $\mathbf{A}$, $\vec{\rho} = Q^t\vec{\phi}$ is the vector containing the normal modes, $d\rho^N = (d\rho_1, d\rho_2, \ldots, d\rho_N)$, k_B is Boltzmann's constant, and T is temperature. Each eigenvalue λ corresponds to a single normal mode. The lowest eigenvalue of $\mathbf{\Lambda}$, $\lambda = 0$, corresponds to the uniform motion, which is treated separately. Therefore, to study only the internal motions, $\lambda = 0$ is removed from $\mathbf{\Lambda}^{-1}$ and the associated column vector is removed from $\mathbf{Q}$. The resulting matrix $\mathbf{Q\Lambda}^{-1}\mathbf{Q}^t$ is also called the pseudoinverse of $\mathbf{A}$ (MathWorks, 1996).

A similar treatment has been developed for bending. There are two independent directions assumed to have the same bending force constant, κ. Due to the mean local cylindrical symmetry, the mean squared amplitudes in both directions are the same. The total bending potential energy is $U = \frac{1}{2}\kappa\vec{\eta}^tA\vec{\eta} + \frac{1}{2}\kappa\vec{\theta}^tA\vec{\theta}$, where κ is the bending force constant. Because there are only N (not $N + 1$) bending angular coordinates, $\vec{\eta}$ and $\vec{\theta}$ are vectors of length N, and $\mathbf{A}$ is now the corresponding $N \times N$ matrix (Wu et al., 1987). By an argument similar to that given in Eq. 1a,

$$\langle \vec{\eta}(\infty)\vec{\eta}^t(\infty)\rangle = \frac{k_BT}{\kappa} Q\Lambda^{-1}Q^t, \tag{1b}$$

where $\mathbf{\Lambda}$ contains $N - 1$ eigenvalues. The uniform mode of motion, for which the eigenvalue is zero, has been removed from both $\mathbf{\Lambda}$ and $\mathbf{Q}$. If we momentarily neglect the difference between N and $N + 1$ beads, then the mean squared amplitudes from the bending and the twisting at the ith base pair, are related through the bending and twisting force constants,

$$\frac{\langle \eta_i(\infty)^2\rangle}{\langle \varphi_i(\infty)^2\rangle} = \frac{\alpha}{\kappa}. \tag{2}$$

For a base pair at the ith position along a chain of $(N + 1)$ units, the mean squared amplitude at infinite time is (Allison et al., 1989; Hustedt et al., 1993a; Wu et al., 1987),

$$\langle \eta_i(\infty)^2\rangle = \frac{k_BT}{\kappa}(Q\Lambda^{-1}Q^t)_{ii}$$

$$\cong \frac{(N+1)k_BT}{12\kappa} f(i, N)$$

$$= \frac{(N+1)h}{12P_{db}} f(i, N), \tag{3}$$

where i ranges from 1 to $(N + 1)$ and

$$f(i, N) \cong \left\{1 + 3\left(\frac{2i - (N+2)}{N+1}\right)^2\right\}, \tag{4}$$

which is nearly a function of $\{i/(N + 1)\}$ only and not of i or N individually. Because $f(i, N)$ increases from 1 to 4 as i varies from $N/2$ to N, the duplex DNA will exhibit four times more amplitude of flexure at the ends than in the center, regardless of length. The dynamic bending persistence length, P_{db}, is related to the dynamic bending force constant κ by

$$\frac{h}{P_{db}} = \frac{k_BT}{\kappa}, \tag{5}$$

where $h = 3.4$ Å is the distance between base pairs. Associated with each mode is a relaxation time. The equations that generate the twisting and bending time constants are given in Eqs. A7, A9, and A15. The relaxation time for the

lth normal twisting mode is

$$\tau(\text{twist})_l = \gamma_t/\alpha\lambda_l, \tag{6}$$

where γ_t is the twisting friction factor. Similarly, the relaxation time for the lth normal bending mode (either in terms of displacements or angles) is then

$$\tau(\text{bend})_l = \gamma_b h_b^2/\kappa_b\lambda_{bl}, \tag{7}$$

where λ_{bl} (defined in Eqs. A14 and A15) is the lth eigenvalue in the matrix Λ_b, and γ_b is the translational friction factor for the spherical bead of diameter h_b. The size of the bead was chosen (Song et al., 1990) to ensure that the uniform modes of the model were consistent with the experimentally determined values. The equations of motion for flexure include the hydrodynamic interaction of the beads (Eq. A13), whereas Eq. 3 needs no hydrodynamic effects. It is not at all obvious that such equations (A13–A15) lead to exactly the same results as Eq. 3 in the infinite-time limit, because neither the set of eigenvalues nor the transformation matrix is the same as the analogous quantities of Eq. 1. Although Eqs. A13 and A15 are quite distinct from Eq. 3, the mean square displacements at infinite time are identical when the transformation matrix is suitably modified (see Eq. A25) and the relaxation times are properly scaled (Eq. A17).

EXPERIMENTAL PROCEDURE (MATERIALS AND METHODS)

The site-specific probe used in this work, Q, is a stable nitroxide radical attached to a modified pyrimidine and base paired with 2-aminopurine, 2AP. Q was prepared as previously described (Miller et al., 1995) using both the naturally abundant [$^{14}N,H_{12}$] and the isotopically substituted [$^{15}N,D_{12}$] nitroxides. The structures of the spin-labeled base pairs, 2AP-Q and A-T*, used previously (Hustedt et al., 1993a, 1995), are shown in Fig. 2 and are compared with the naturally occurring base pairs, AT and GC. Oligomers were prepared on an ABS 392 DNA synthesizer, sized with denaturing polyacrylamide gel electrophoresis (dPAGE), and purified on a Sephadex column, or purified by trityl-on reverse-phase high pressure liquid chromatography (HPLC) and the trityl removed by 85% glacial acetic acid in water. The spin-labeled sequences were then combined with a 10–50% excess of the corresponding unlabeled complementary strand. Total concentrations ranged from 60 to 500 μM duplex DNA. The buffer (PNE) in all cases was 10 mM sodium phosphate (pH 7.0), 0.1 mM EDTA, and 0.1 M NaCl. The EPR spectra were recorded digitally on an EPR 9.4-GHz spectrometer previously described (Mailer et al., 1985, 1991), and a commercial Bruker EMX spectrometer (Bruker, Inc., Billerica, MA). EPR parameters were 10 and 100 kHz modulation frequency, 1.0 G modulation amplitude, and 1 and 2 mW microwave power (nonsaturating conditions). Temperature was regulated to $\pm 0.2°$. Samples were kept in a refrigerator at 4°C between measurements. EPR spectra were recorded within 2 weeks of sample preparation.

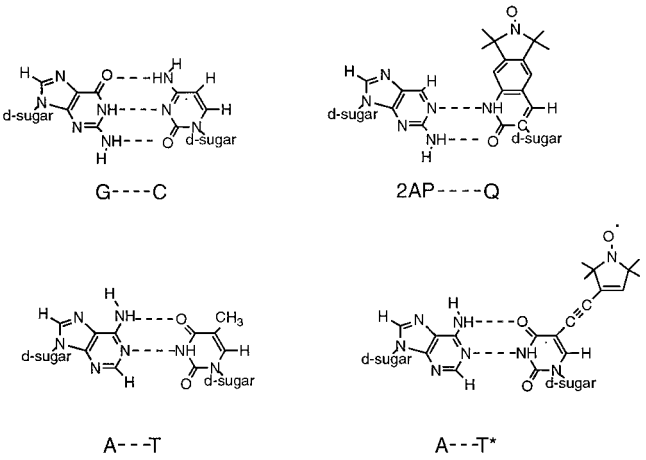

FIGURE 2 Spin-labels T* and Q, incorporated into base pairs A-T* and 2AP-Q. The native base pairs A-T and G-C are shown for comparison.

TABLE 1 Sequences for non self-complementary middle-labeled DNA with the EPR-active spin-label Q

$N + 1$	Sequence
14	5′-d(GAC CTC GQA TCG TG)
28	5′-d(ATG GTG C-[14-mer]-ATG GTG C)
50	5′-d(TAA TCT ATC GT-[28-mer]-TCT TCG TGT CC)
100	5′-d(TAC GAA CCT GAG CTA TTT CCC GGC T-[50-mer]-GGA AAG GTG GTG CTC ACT GGA GCA A)

Each duplex used the sequence given here with its 2AP-containing complementary strand. The basic template came from the *Drosophila melanogaster* TATA-box binding protein TFIID gene, positions 1062 to 1151, where the A at position 1112 was replaced with Q, the spin-label. The sequence was chosen to have approximately a 1:1 ratio of GC and AT base pairs, and also to avoid known oddities such as long runs of a single base.

Four DNA duplexes, of lengths $N + 1 = 14$, 28, 50, and 100 base pairs, were designed such that each carried one spin-label Q in the middle position and are explicitly listed in Table 1 and schematically illustrated in Table 2. The local base sequence about Q (6 base pairs including Q: TCGQAT) was conserved in each of the 14-mers; the 14-mer sequence middle containing Q was conserved in each of the 28-mers; the 28-mer middle containing Q was conserved in the 50-mers; and the 50-mer middle containing Q was conserved in the 100-mers, while both DNA sequence length and probe position were varied. Each middle-labeled ($N + 1$ base pair) sequence was cyclically permuted so that, when the spin-label was in position i, the fractional position, $i/(N + 1)$, was nearly maintained. This is schematically illustrated in Table 3 for the 28-mers. The values of $f(i, N)$, Eq. 4, are available in Table 4.

Obtaining internal dynamics from EPR spectra

The protocol described in detail by Hustedt et al., (1993a) and used here to extract the internal dynamics of DNA was as follows. The EPR spectra of DNA in PNE buffer were simulated using slow-motion density matrix theory. The **A** (splitting) and **g** chemical shift anisotrophy (CSA) tensors, the homogeneous line width, the inhomogeneous line width, the orientation of the principal axis of the **A** and **g** tensors of the spin probe relative to the helix axis of the DNA (θ_{tilt}), and the correlation times for the uniform modes of motion were required for the analysis. The correlation times, given in Table 5, were calculated by $\tau_{\|} = 1/6D_{\|}$ and $\tau_{\perp} = 1/6D_{\perp}$. The diffusion coefficients for the uniform modes, $D_{\|}$ and $D_{\perp}$, were calculated

TABLE 2 Schematic of length-dependence labeling strategy of Table 1

	Length Series
14-mer:	—Q—
28-mer:	——(14-mer)——
50-mer:	———(28-mer)———
100-mer:	————(50-mer)————

TABLE 3 Schematic of position dependence labeling strategy, illustrating the cyclic permutation of sequence to move Q from the middle to either the left or right position

	Position Series for the 28 Base Sequences
Left	5′-d(**GAC CTC GQA TCG TG**C TCC TCA ATG GTG C)
Middle	5′-d(ATG GTG C**GA CCT CGQ ATC GTG** CTC CTC A)
Right	5′-d(CTC CTC AAT GGT GC**G ACC TCG QAT CGT G**)

Each Q-labeled strand was matched with its 2AP-containing complementary strand. Cyclic permutation means figuratively joining the ends of the sequence to make a circle, then cutting the circle independently in three different places to create the three different position members of each length sequence. The 28-mer sequences are shown. The 14-mer sequence is in bold.

from the theory of Tirado and Garcia de la Torre for a right circular cylinder of radius $R = 12$ Å and length $3.4 \times (N + 1)$ Å, where $N + 1$ is the number of base pairs (Eimer et al., 1990; Hustedt et al., 1993a; Tirado and Garcia de la Torre, 1980).

The no-motion **A** and **g** tensors, used to describe the interaction of the electron spin with the nitrogen nuclear spin and the magnetic fields, respectively, were obtained from left-, middle-, and right-[^{15}N,D$_{12}$] spin-labeled samples of 14-mer duplex DNA in 50% w/v sucrose in PNE buffer (representative spectra are shown in Fig. 3). Spectra were obtained at 0°C from the DNA in the high sucrose buffer, where all relaxation times are increased by a factor of 30 from those at 20°C in 0% sucrose in PNE. Under such conditions, some of the internal motion is removed, and the uniform modes are slow enough that, effectively, the EPR spectra are in the no-motion (or powder pattern) limit. The rigid limit **g** tensors were obtained by a best-fit to 94 GHz powder pattern spectra and then fixed. The rigid limit **A** tensors were obtained by a best-fit to both 9.4 and 94 GHz powder pattern spectra using the rigid limit **g** tensors found as described above (Hustedt et al., 1993b). The inhomogeneous and homogeneous line widths for each nuclear manifold were also allowed to vary. The **A** tensor elements for the [^{14}N,D$_{12}$] spin-label were calculated from the **A** tensors for the [^{15}N,H$_{12}$] spin-label by the relation: $\mathbf{A}([^{14}\mathrm{N,H}_{12}]) = 0.7131 \times \mathbf{A}([^{15}\mathrm{N,D}_{12}])$, while the **g** tensors were taken to be the same for both isotopic forms of the spin-label. **A** and **g** tensors were individually determined for the left-, middle-, and right-labeled 14-mer DNAs in 50% sucrose solution and applied to the corresponding 14-, 28-, 50-, and 100-mer left-, middle-, and right-labeled DNAs in PNE and 0% sucrose solution spectra. A single set of **A** and **g** tensors, used to simulate all of the data of Fig. 3, failed to adequately fit the experimental spectra. Therefore, we allowed the left-, middle-, and right-labeled DNAs each to be fitted by an individual set of motion-independent tensors. The values of the **A** and **g** tensors, given in Table 6, are obtained by assuming that there is some residual motion in the spectra of the samples in 50% sucrose, with a mean square amplitude of 0.012 rad^2 independent of label position, according to Eq. 8 below. Finally, we assume that the collective modes contribute very little to the residual motion of the base pairs in the 14-mer in 50% sucrose. The homogeneous and inhomogeneous line widths were individually adjusted for the spectra of the DNA in 0% sucrose PNE buffer. The tilt angle, θ_{tilt}, was experimentally estimated to be 20°, from both two-dimensional (2D) NMR distance geometry measurements and EPR simulations (Alley, 1996), and was fixed at this value; this is the same tilt angle found for an earlier spin probe T* (Reese, 1996; Reese et al., 1996a,b).

TABLE 4 Position (*i*) of the spin-label Q in the duplex DNA molecules of length $N + 1$ base pairs, and the value of $f(i, \mathrm{N})$ for that position and length of the duplex DNA.

$N + 1$	i(left)	$f(i, \mathrm{N})$	i(middle)	$f(i, \mathrm{N})$	i(right)	$f(i, \mathrm{N})$
14	4	1.75	8	1.01	12	2.24
28	8	1.65	15	1.00	22	1.86
50	13	1.75	26	1.00	39	1.87
100	26	1.72	51	1.00	76	1.78
50	6	2.83				

The parameter, $\langle\beta_i^2\rangle$, is the mean square oscillation due to the internal dynamics, both collective and local, of a spin-label attached to a base at position i in the duplex DNA. We assume that the underlying distribution of angles about the mean is symmetric and Gaussian. When the internal motion is rapid, the **A** and **g** tensors are averaged. For the **A** tensor, rapid motions average the tensor to give (Hustedt et al., 1993a)

$$\begin{pmatrix} \langle A_{xx}\rangle \\ \langle A_{yy}\rangle \\ \langle A_{zz}\rangle \end{pmatrix} = \left\{1 + \frac{1}{2}\langle\beta_i^2\rangle \begin{pmatrix} -1/2 & -1/2 & 1 \\ -1/2 & -1/2 & 1 \\ 1 & 1 & -2 \end{pmatrix}\right\} \begin{pmatrix} A_{xx} \\ A_{yy} \\ A_{yz} \end{pmatrix}. \tag{8}$$

with a similar expression for the **g** tensor. It is assumed that the amplitude of motion is limited ($\sqrt{\langle\beta_i^2\rangle} < 20°$) and is applicable to both 1-dimensional (1D) and 2D models of the dynamics. An order parameter, S_i, may be calculated,

$$\begin{aligned} S_i &= \frac{\langle A_{zz}\rangle - \bar{a}}{A_{zz} - \bar{a}} = \frac{3\langle\cos^2\theta\rangle - 1}{2} \\ &= \frac{3\exp\{-2\langle\beta_i^2\rangle\} + 1}{4} \approx 1 - \frac{3}{2}\langle\beta_i^2\rangle, \end{aligned} \tag{9}$$

where $\bar{a}$ is the mean value of the three tensor elements and is independent of the averaging effects shown in Eq. 8. $\langle\beta_i^2\rangle$ was found by comparing the simulation using the averaged tensors with the experimental data. Fitting was performed on the outer wings of the spectra until there was optimal agreement between the simulated and experimental spectra. The optimization process maximizes the correlation coefficient R, (minimizing χ^2) (Hustedt et al., 1993a). Values of $R \geq 0.97$ were obtained in all cases where $\langle\beta_i^2\rangle$ is reported.

Analysis of internal dynamics as a function of length and position

The effective averaging of a base pair due to internal motions comes from two sources; the collective bending modes, $\langle\eta_i^2\rangle$, and the independent local motion of the base pair (containing the nitroxide), $\langle\beta_o^2\rangle$, which is assumed to be independent of position and length of the DNA. We assume that the mean-squared amplitudes of these motional processes are additive (Hustedt et al., 1993a),

$$\langle\beta_i^2\rangle = \langle\eta_i^2\rangle + \langle\theta_i^2\rangle + \langle\beta_o^2\rangle = 2\langle\eta_i^2\rangle + \langle\beta_o^2\rangle. \tag{10}$$

The length-dependent contribution is purely bending and is two-dimensional. The length-independent contribution may be 1D, 2D, or three-dimensional (3D).

The effects of twisting on the total amplitude

Eq. 8 was developed by assuming that the **A** tensors were coincident with the helix axis and that twisting could be neglected. In fact, however, the spin probe is tilted from the helix axis by about 20°. We can calculate the motionally averaged tensors including both twisting and flexing by averaging a limited amplitude of motion about an arbitrary axis (Hustedt et al., 1993a; Van et al., 1974). The true **A** (or **g**) tensor is rotated, by a Eulerian rotation, Ω, consisting of 3 Euler angles, so that the spin-label is aligned with the axis of libration,

$$A' = R(\Omega)AR^{\mathrm{t}}(\Omega), \tag{11}$$

where the R matrices are defined by Goldstein (1975) and Hustedt et al. (1993a). Dynamic rotation by angle ξ, in terms of a rotation around the new

TABLE 5 Time constants, in nanoseconds, from theory for DNA of length 3.4 * (*N* + 1) Å and radius 12.0 Å, in 0% sucrose and 50% sucrose, at *T* = 0, 10, 20, 30, 40°C

	T									
	0°C		10°C		20°C		30°C		40°C	
N + 1	$\tau_\perp$	$\tau_\parallel$	$\tau_\perp$	$\tau_\parallel$	$\tau_\perp$	$\tau_\parallel$	$\tau_\perp$	$\tau_\parallel$	$\tau_\perp$	$\tau_\parallel$
0% w/v sucrose										
11	12.32	6.95	8.73	4.92	6.47	3.65	4.97	2.81	3.94	2.22
12	14.32	7.45	10.14	5.28	7.52	3.91	5.78	3.01	4.58	2.38
14	18.82	8.44	13.34	5.98	9.89	4.43	7.60	3.41	6.02	2.70
15	21.35	8.92	15.13	6.32	11.22	4.69	8.62	3.60	6.83	2.85
20	37.21	11.33	26.37	8.03	19.55	5.95	15.03	4.57	11.90	3.62
22	45.18	12.28	32.02	8.70	23.74	6.45	18.24	4.96	14.45	3.93
28	75.37	15.11	53.41	10.71	39.59	7.94	30.43	6.10	24.10	4.83
30	87.68	16.05	62.13	11.38	46.06	8.43	35.41	6.48	28.04	5.13
50	284.4	25.42	201.5	18.01	149.4	13.35	114.8	10.26	90.92	8.13
60	441.4	30.08	312.8	21.32	231.9	15.80	178.3	12.15	141.2	9.62
100	1578	48.7	1118	34.5	828.8	25.59	637.1	19.67	504.4	15.58
η*	1.78		1.31		1.00		0.80		0.65	
50% w/v sucrose										
11	309.6	174.7	168.1	94.80	99.44	56.09	63.02	35.55	42.22	23.82
12	359.8	187.3	195.3	101.6	115.6	60.13	73.24	38.11	49.07	25.53
14	473.0	212.0	256.7	115.1	151.9	68.09	96.27	43.16	64.50	28.91
15	536.7	224.3	291.3	121.7	172.4	72.03	109.2	45.65	73.18	30.58
20	935.3	284.7	507.6	154.5	300.4	91.43	190.4	57.94	127.5	38.82
22	1136	308.6	616.4	167.5	364.7	99.11	231.2	62.81	154.9	42.08
28	1894	379.9	1028	206.2	608.4	122.0	385.6	77.32	258.3	51.80
30	2204	403.5	1196	219.0	707.8	129.6	448.6	82.13	300.5	55.03
50	7148	638.9	3879	346.7	2295	205.2	1455	130.0	974.7	87.12
60	11096	756	6022	410.4	3563	242.8	2258	153.9	1513	103.1
100	39655	1224	21522	665	12735	393	8071	249.2	5408	167.0
η*	44.7		25.2		15.4		10.1		7.0	

From Tirado and Garcia de la Torre, 1980.
*η is viscosity in cP.

z-axis, is carried out by the rotation matrix,

$$R_\xi = \begin{pmatrix} \cos\xi & \sin\xi & 0 \\ -\sin\xi & \cos\xi & 0 \\ 0 & 0 & 1 \end{pmatrix}. \quad (12)$$

The dynamically averaged **A** tensor is $\langle A' \rangle = \langle R_\xi A' R_\xi^t \rangle$, which can be written specifically as

$$\langle A' \rangle = A' - B' \quad (13)$$

where

$$B' = \begin{pmatrix} \mu(A'_{11} - A'_{22}) & 2\mu A'_{12} & \tfrac{1}{2}(1-\nu)A'_{13} \\ 2\mu A'_{12} & -\mu(A'_{11} - A'_{22}) & \tfrac{1}{2}(1-\nu)A'_{23} \\ \tfrac{1}{2}(1-\nu)A'_{13} & \tfrac{1}{2}(1-\nu)A'_{23} & 0 \end{pmatrix}$$

and $\mu = \langle \sin^2 \xi \rangle$ and $\nu = \langle \cos \xi \rangle$. We may find $\langle A \rangle$ by rotating back into the original frame,

$$\langle A \rangle = R^t(\Omega)\langle A' \rangle R(\Omega) = A - R^t(\Omega)B'R(\Omega). \quad (14)$$

When the underlying distribution is Gaussian, with variance $\langle \xi^2(\infty) \rangle$, it follows that the quantities μ and ν depend on a single parameter $\langle \xi^2(\infty) \rangle$,

$$\mu = \tfrac{1}{2}(1 - \exp\{-2\langle \xi^2(\infty) \rangle\})$$

and

$$\nu = \exp\{-\tfrac{1}{2}\langle (\xi^2(\infty)) \rangle\}.$$

For small amplitude averaging, $\mu = \langle \xi^2(\infty) \rangle$ and $(1 - \nu) = \tfrac{1}{2} \cdot \mu$, and the B' matrix is proportional to μ. Small amplitude averaging makes the $\|B'\|$ small and the averaged **A** tensor matrix, $\langle A \rangle$, is nearly diagonal when transformed back into the original frame. When Eq. 13 is applied to the case for 2D flexural motion (in which the two axes of flexural motion are perpendicular to the axis of the spin-label), then $\mu = \langle \beta^2(\infty) \rangle$, and the result is Eq. 8. We can use Eqs. 12–14 to include the effect of the torsional motion on the **A** and **g** tensors; Eq. 12 must be applied twice to obtain the result. In the first averaging, the spin-label is tilted by $\theta_{tilt} = 20°$, and averaged by $\langle \phi_i(\infty)^2 \rangle$. Eq. 2 gives $\langle \phi_i(\infty)^2 \rangle = \langle \eta_i(\infty)^2 \rangle (\kappa/\alpha)$, where the quantities on the right-hand side can be estimated ($\kappa/\alpha = 3.75$) (Robinson et al., 1997; Schurr et al., 1992). Second, the resultant tensor is tilted by 70° and averaged over the bending (about both axes). This is compared with the effects of just tilting by 90° and averaging over the two librational axes for bending (Eq. 8).

RESULTS

Table 1 lists the specific sequences of the middle-labeled duplex DNA studied. Tables 2 and 3 schematically illustrate the labeling schemes used. Each duplex has $N + 1$ base pairs and is referred to as an $(N + 1)$-mer. EPR spectra of the 14-mer DNA duplexes in 50% sucrose and PNE buffer are shown in Fig. 3, along with simulations that assume no dynamics. Spectra are shown in Fig. 4 for the [^{15}N,D_{12}]-labeled and [^{14}N,H_{12}]-labeled DNA duplexes in PNE at 0°C, for left-labeled ($f(i, N) \cong 1.75$, see Table 4) (N +

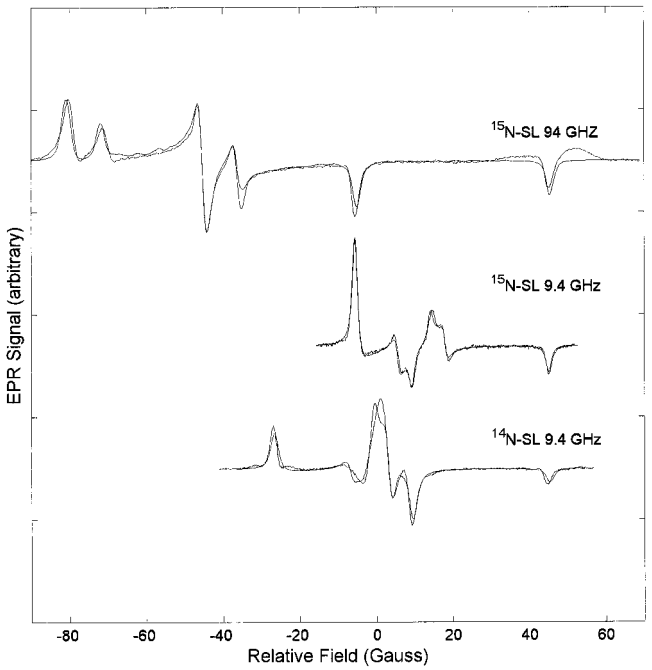

FIGURE 3 9.4 and 94 GHz CW-EPR spectra of rigid-limit 14-mers of duplex DNA labeled with Q in 50% w/v sucrose in PNE at 0°C. (*Top*) [^{15}N,D$_{12}$] left-labeled 94 GHz spectrum. (*Middle*) [^{15}N,D$_{12}$] middle-labeled 9.4 GHz spectrum. (*Bottom*) [^{14}N,H$_{12}$] left-labeled 9.4 GHz spectrum. These spectra and the remaining left-, middle-, and right-labeled 14-mer analogs in 50% w/v sucrose in PNE at 0°C were fit to the tensors given in Table 6 corresponding to their label position. The average homogeneous center line width for [^{14}N,H$_{12}$] left-, middle-, and right-labeled DNA was 0.85 G with a 0.58 G inhomogeneous broadening. The homogeneous line widths for low- and high-field lines for the [^{15}N,D$_{12}$] left-, middle-, and right-labeled DNA at 94 GHz were, on average, 0.87 G and 0.80 G, respectively, with 0.7 G and 0.58 G inhomogeneous broadening. The homogeneous line widths for low- and high-field lines for [^{15}N,D$_{12}$] left-, middle-, and right-labeled DNA at 9.4 GHz were, on average, 0.84 G and 0.90 G with 0.00 G inhomogeneous broadening. EPR spectra of right-labeled DNA are not shown. The correlation coefficient, R, defined elsewhere (Hustedt et al., 1993a), was between 0.97 and 0.99 for each simulation.

1)-mers. Simulations were performed using the $\tau_{\parallel}$ and $\tau_{\perp}$ values given in Table 5. Only the homogeneous linewidths and $\langle\beta_i^2\rangle$, the measure of internal dynamics, were adjusted to optimize the fit of the simulations to the data; all other parameters were fixed.

Analysis of bending amplitude as a function of length and position

Eqs. 3 and 10 predict that the values of $\langle\beta_i^2\rangle$ depend on both the label position and the total number of base pairs in the duplex DNA. The theory of Eqs. 3 and 10 suggests that $\langle\beta_i^2\rangle$ should be approximately a linear function of $(N + 1)$. In Fig. 5, the mean squared amplitudes of oscillation $\langle\beta_i^2\rangle$, obtained from the spectra as illustrated in Fig. 4, are plotted as a function of length for the left-, middle-, and right-labeled $(N + 1)$-mers, from spectra of 14 to 100 base pairs at 0°C. The values of $\langle\beta_i^2\rangle$, for the middle-labeled case, $i \approx$ ½$(N + 1)$, are linearly related to $N + 1$. The best, least squares linear relation between $\langle\beta_i^2\rangle$ and $(N + 1)$ is shown for each data set, independently. However, the mean squared amplitudes of the left- and right-labeled DNAs depart markedly from linearity above 50 base pairs. Therefore, the data for the left- and right-labeled DNAs at 100 base pairs are neglected, for the moment, from the linear fits in Fig. 5. From these slopes, an approximate bending force constant of $\kappa = 1.61 \times 10^{-11} \pm 0.08 \times 10^{-11}$ ergs/rad^2 can be estimated for the middle-labeled DNA. Similarly, κ is $1.23 \times 10^{-11} \pm 0.09 \times 10^{-11}$ ergs/rad^2 for the left-labeled DNA, and $\kappa = 1.23 \times 10^{-11} \pm 0.05 \times 10^{-11}$ ergs/rad^2 for the right-labeled DNA at 0°C.

TABLE 6 Rigid-limit tensor elements used for all simulations.

	x	*y*	*z*
left			
g	2.0089	2.0068	2.0031
A(14N) G	6.13	6.00	36.45
A(15N) G	8.60	8.42	51.12
middle			
g	2.0086	2.0064	2.0026
A(14N) G	5.81	5.75	36.75
A(15N) G	8.15	8.07	51.53
right			
g	2.0087	2.0066	2.0029
A(14N) G	6.24	6.03	36.29
A(15N) G	8.75	8.45	50.89

Tensors were constrained such that $\mathbf{A}(^{14}\text{N}) = 0.7131 \times \mathbf{A}(^{15}\text{N})$.

We now consider why the values of $\langle\beta_i^2\rangle$ (Fig. 5) depart from the linear dependence on $N + 1$ as predicted by Eq. 3 for the left- and right-labeled cases, but not for the middle-labeled case when $N + 1$ is between 50 and 100 base pairs. One possible explanation is that the modes of motion are in the intermediate time regimen of linear CW-EPR and are not sufficiently rapid to fully average the tensors. This requires that we now examine the predictions of the theory of the weakly bending rod to estimate the time constants of the various modes.

The time constants for the internal dynamics due to twisting, $\tau_{(\text{twist})}$, and bending, $\tau_{(\text{bend})}$, were calculated from Eqs. 6 (Allison et al., 1989; Wu et al., 1987) and 7 (Song et al., 1990), respectively. The time constants for the four longest motional modes as a function of DNA length are shown in Fig. 6, for bending (Fig. 6, *a* and *c*) and twisting (Fig. 6, *b* and *d*), calculated with the parameters corresponding to PNE buffer at 20°C (Fig. 6, *a* and *b*) and 50% sucrose w/v in PNE buffer at 0°C (Fig. 6, *c* and *d*). Note that $\tau_{(\text{bend})}$ of the longest bending mode (0% sucrose, 20°C) exceeds 10 nanoseconds at (and above) 60 base pairs duplex DNA. This is slower than the fast motion limit and should be excluded, or partially excluded, from the calculation of $\langle\eta_i^2\rangle$. The $\tau_{(\text{bend})}$ for the second longest mode exceeds 10 ns at about 110 base pairs. For middle-labeled DNA, the longest mode (the fundamental or horseshoe shaped mode) contributes only to translational relaxation and not at all to rotational

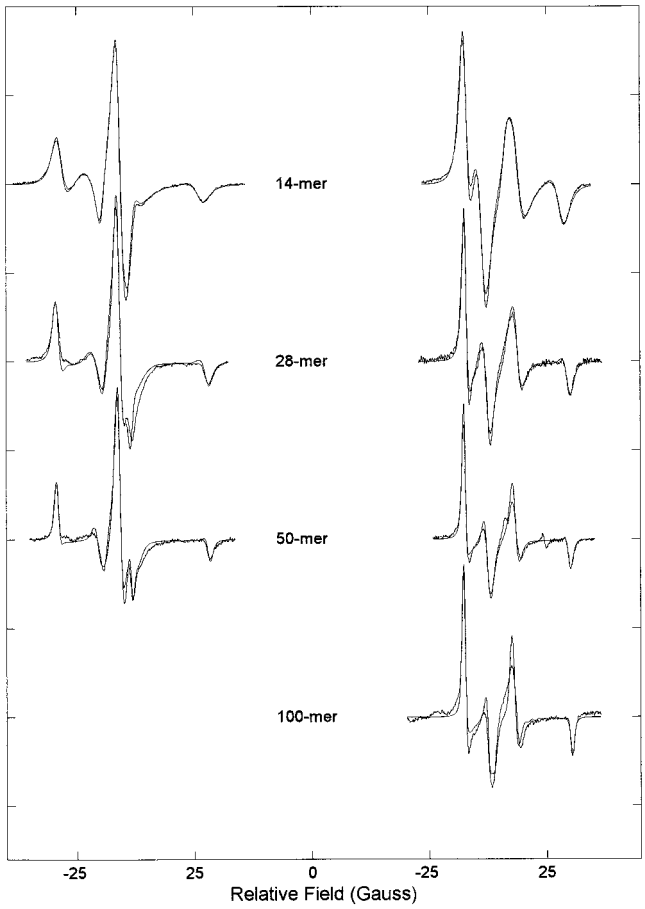

FIGURE 4 Spectra of [$^{14}N,H_{12}$] (*left column*) and [$^{15}N,D_{12}$] (*right column*) left spin-labeled ($N + 1$)-mer duplex DNA at 0°C in PNE buffer, with simulations overlaid. The **A** and **g** tensors are given in Table 6; the correlation times are given in Table 5. A 20° tilt angle was used; homogeneous line widths and $\langle\beta_i^2\rangle$ were optimized to fit the simulations to spectra. The values of $\langle\beta_i^2\rangle$ are

	^{14}N	^{15}N
14-mer	0.0196	0.0260
28-mer	0.0286	0.0366
50-mer	0.0432	0.0444
100-mer		0.0545

relaxation. In contrast, the second longest mode contributes considerably to the middle-labeled DNA's rotational relaxation. However, for the left- and right-labeled DNA, the longest mode contributes more than half that of the total rotational relaxation. $\tau \cdot \Delta A < 1$ conventionally represents the fast motion limit, where τ is the time constant of the dynamics process and ΔA is the distance between spectral lines, in Hz, that the motion averages (Hustedt et al., 1993a; Nordio, 1976). For spin-labels, whenever τ of a process is longer than a few nanoseconds, the EPR spectrum is not in the fast motion limit. Consequently, because the longest mode contributes more to the relaxation of the left- and right-labeled DNA, the deviation from linearity should begin around 60–70 base pairs. For the middle-labeled DNA, deviation from linearity should begin around 110 base pairs. This qualitatively explains why the middle-labeled DNAs do not appear to markedly deviate from linearity, as do the left- and right-labeled DNAs.

The above argument qualitatively demonstrates that modes with long correlation times do not cause as much spectral-position averaging as do modes with the same amplitude but faster correlation times. This argument can be made more quantitative. We can lessen or down-weight the contribution to the spectral-position averaging of modes whose dynamics are too slow for rapid pre-averaging. Eq. 3 can be modified to weight differently the contribution of the individual modes to the calculation of $\langle\eta_i^2\rangle$,

$$\langle\eta_i(\infty)^2\rangle = \frac{k_B T}{\kappa}\sum_{l=1}^{N-1} w_{i,l} Q_{il}^2 \lambda_l^{-1}, \tag{15}$$

where we take a phenomenological functional form for the weighting factors,

$$w_{i,l} = \exp\{-\tau_l \cdot \Delta A_{i,l}\}. \tag{16}$$

In Eq. 16, $w_{i,l}$ is a weighting factor that depends on the relaxation time of the lth motional mode and on the dynamics of a spin-label attached to the ith base pair (see Eq. A17). When the relaxation time is very fast, the weighting factor for each mode is one and decreases toward zero as the relaxation time of the associated mode increases. We can estimate ΔA from the approximate resonance condition (Griffith and Jost, 1976):

$$A(\theta) = A_{zz}\cos^2\theta + A_\perp \sin^2\theta$$

or

$$\Delta A = A(\theta) - A(0) \approx (A_\perp - A_{zz})\sin^2\theta.$$

The total angular displacement is $|\theta| = \sqrt{2\langle\eta_i(\infty)^2\rangle}$, for an individual mode. Therefore,

$$\Delta A_{i,l} = \left|(A_\perp - A_{zz})\sin^2\left(\sqrt{2\frac{k_B T}{\kappa} Q_{il}^2 \lambda_l^{-1}}\right)\right|. \tag{17}$$

For the typical amplitudes of motion and tensors (Table 6) the maximum relaxation time for which the fast motion assumption will be valid is on the order of nanoseconds. To see how well the weighted, weakly bending rod theory accounts for the data, the $\langle\beta_i^2\rangle$ of Fig. 7 are compared with theoretical values obtained using Eq. 10 and the $\langle\eta_i^2\rangle$ calculated from Eq. 15, with no adjustable parameters. The $\tau_{(\text{bend})_l}$ were calculated from Eqs. 7 and A17. The bending force constant κ and the length-independent contribution $\langle\beta_o^2\rangle$ were those obtained from the middle-labeled DNA at 0°C (see Fig. 5 legend). The results of the weighted fitting are shown in Fig. 7.

The small dots in Fig. 7 are the theoretical values of $\langle\beta_i^2\rangle$ as a function of length, calculated with the weighted, weakly bending rod theory (Eq. 15). The weighting accounts nicely for the deviation in the data seen for the left- and right-labeled 100-mers. Even the 50-mer, consisting of

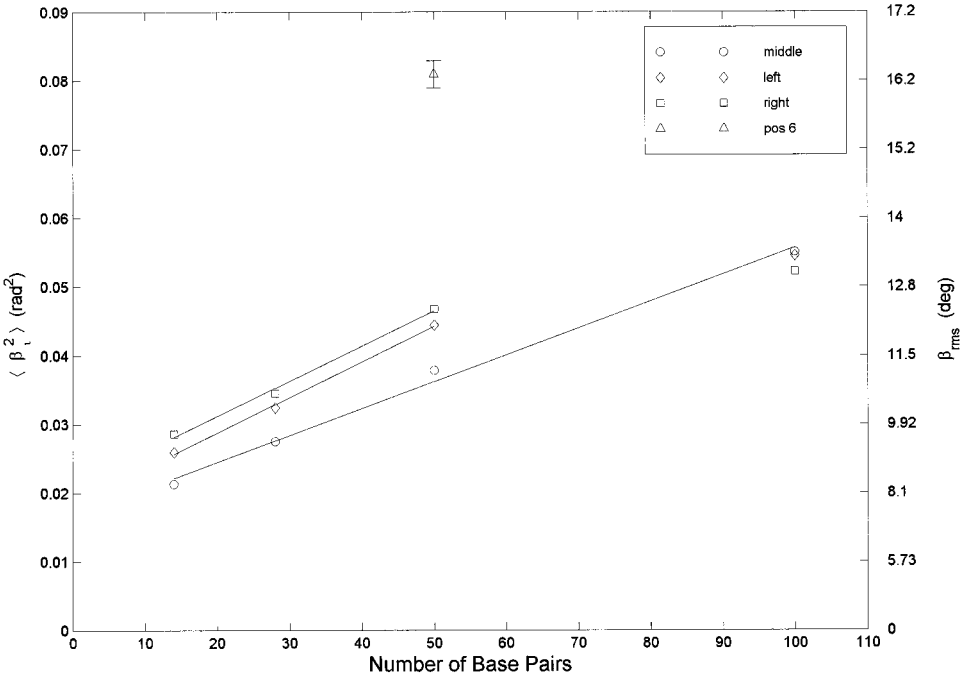

FIGURE 5 The mean squared oscillation parameter $\langle\beta_i^2\rangle$ (rad^2), and the r.m.s. angular displacements β_{rms}(deg) on right-hand axis due to the internal dynamics of DNA, as a function of $N + 1$ base pairs of duplex DNA labeled on the right (□) ($i \approx \frac{3}{4}N$), the middle (○) ($i \approx \frac{1}{2}N$), and the left (◇) ($i \approx \frac{1}{4}N$), and a 50-mer labeled at position 6 (△) ($i \approx \frac{1}{10}N$) all at $T = 0$°C. Each data set is least-squares fit to the linear model, where $\langle\beta_i^2\rangle$ depends linearly on $(N + 1)$ (as suggested by combining Eqs. 3 and 10). Each fit is shown by its respective solid line. The slopes and intercepts are

	Left	Middle	Right
Slope (rad^2/bp) $*$ 10^3	0.51 ± 0.02	0.39 ± 0.02	0.51 ± 0.04
Intercept (rad^2)	0.0185 ± 0.0005	0.0167 ± 0.0004	0.0210 ± 0.0005

The left- and right-labeled 100-mer DNAs and the 50-mer labeled at position 6 were not included in the fits. Errors for $\langle\beta_i^2\rangle$ are reported as $\pm 1\sigma$.

a different sequence of DNA labeled at position 6, is reasonably well accounted for by the theory. At each N, the increasing order of the simulated $\langle\beta_i^2\rangle$ for left-, middle-, and right-labeled DNA is the same as the experimental $\langle\beta_i^2\rangle$ for the left-, middle-, and right-labeled DNA. The solid and dashed lines that go near the dots in Fig. 7 are approximate theoretical values of $\langle\beta_i^2\rangle$ as a function of length, calculated using approximately constant i/N values and are drawn only to help the reader visualize the dependence of $\langle\beta_i^2\rangle$ on probe position and DNA length. At small values of N, the slopes of the left- and right-labeled DNA lines are approximately twice as steep as that of the middle-labeled DNA line, in good agreement with the theory (Eq. 4), which predicts a ratio of approximately 1.8. The constraint that all curves must come to a single value of $\langle\beta_o^2\rangle$ in the limit as $(N + 1)$ goes to zero may be too harsh a constraint, because different positioning of the labels and different sequences may not extrapolate to the same point. Nonetheless, the model was constrained with this criterion.

We used the weighted, weakly bending rod theory to obtain an optimized persistence length that uses all of the data shown in Fig. 7. We performed a least squares optimization of the theory in Eqs. 10 and 15 on the data for the left-, middle-, and right-labeled DNAs. We allowed the bending force constant, the single intercept $\langle\beta_o^2\rangle$, and a single scale factor on all of the bending relaxation times (see Eq. A17) to vary to obtain an optimized fit. The bending force constant increased by around 15%. The results are given in the legend of Fig. 7.

Figure 8 overlays EPR spectral simulations and data for the middle-labeled 28-mers in PNE and 0% sucrose from 0 to 40°C. How the width of the spectra systematically pull in and $\langle\beta_i^2\rangle$ increases with increasing temperature is illustrated. The predicted rates of the uniform modes also increase, as given in Table 5. In Fig. 9, $\langle\beta_i^2\rangle$, as a function of length for only the middle-labeled DNA, is shown at temperatures of 0, 10, 20, 30, and 40°C. Fitting all the data shown in Fig. 9, except for the two high-temperature 14-mers, and assuming a single T independent bending constant gives a value $\kappa = 1.44 \times 10^{-11} \pm 0.04 \times 10^{-11}$ ergs/rad^2. The low-temperature data (0–10°C) considered separately are best-fitted by a bending constant $\kappa = 1.62 \times 10^{-11} \pm 0.05 \times 10^{-11}$ ergs/rad^2. The high-temperature data (30 and 40°C) are best-fitted by $\kappa = 1.27 \times 10^{-11} \pm 0.08 \times 10^{-11}$ ergs/rad^2. The ratio of bending force constants from the low-temperature data to those of the high-temperature data is about 1.2, indicating that the bending force constant may be temperature dependent. The intercepts, i.e., the values of the $\langle\beta_o^2\rangle$, at each temperature determined from the single bending constant model were, to within experimental error, the same as

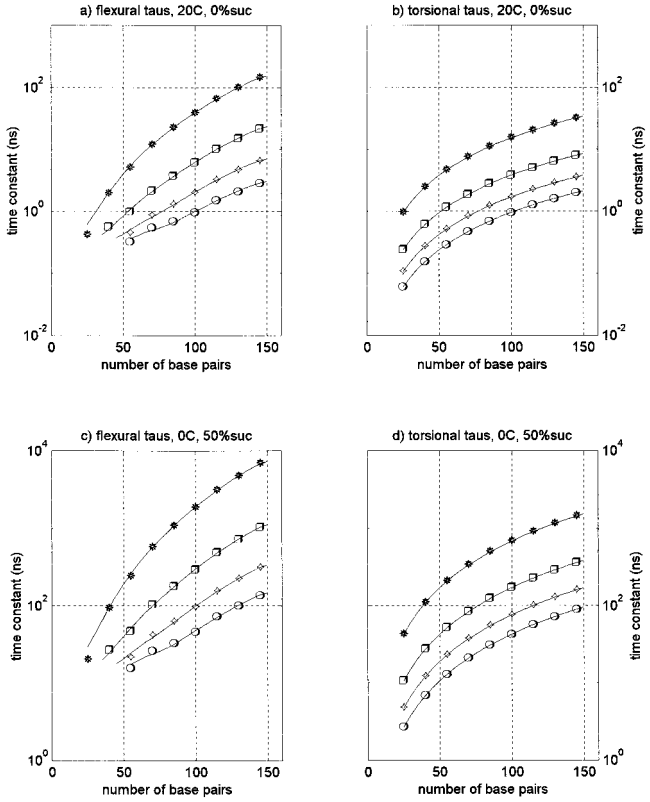

FIGURE 6 Time constants of the first four internal modes of motion for both torsional and flexural dynamics as a function of the number of base pairs, using $P_{db} = 1250$ Å, $h = 3.4$ Å, and computed from Eqs. 6 and 7. (*a*) Flexural, $\tau_{(bend)_l}$, 20°C, 0% sucrose. (*b*) Torsional, 20°C, 0% sucrose. (*c*) Flexural, 0°C, 50% sucrose. (*d*) Torsional, $\tau_{(twist)_l}$, 0°C, 50% sucrose. The torsional force constant $\alpha = 4 \cdot 10^{-12}$ ergs/rad^2 and torsional friction factors $\gamma_t = 6 \cdot 10^{-23}$ erg · sec/rad^2 in PNE at 20°C and $\gamma_t = 2.7 \cdot 10^{-21}$ erg · sec/rad^2 in 50% sucrose w/v in PNE at 0°C were used. Calculation of the bending time constants using the scaled model, in which $N_b + 1$ beads with radius 15.9 Å replaced $N + 1$ base pairs, are discussed in the Appendix. In 0% sucrose w/v in PNE at 20°C, bending constant $\kappa = 1.5 \times 10^{-11}$ erg/rad^2 and bending rotational friction factor $\gamma_{rb} = 3\pi\eta h_b^3 = 3.0 \times 10^{-21}$ erg · sec/rad^2 were used; and in 50% sucrose w/v in PNE at 0°C $\gamma_{rb} = 1.4 \times 10^{-19}$ erg · sec/rad^2.

those obtained from the best-fit straight line of each of the data sets at each temperature.

Figure 10 shows DNA length independent $\langle\beta_o^2\rangle$ as a function of temperature. The values of $\langle\beta_o^2\rangle$ were obtained from the data of Fig. 9 (see legend) and depend approximately linearly on temperature over the small (40°) temperature range. However, fitting of $\langle\beta_o^2\rangle$ to a linear function of temperature cannot be a complete description, because it provides no insight into the limiting value of $\langle\beta_o^2\rangle$ at extremely low temperatures. We suggest that $\langle\beta_o^2\rangle$ may be described by a model in which the motion of the probe is constrained by a simple harmonic well (see legend for model). Figure 10 shows a fit (*dotted line*) of this model to the $\langle\beta_o^2\rangle$. The model does not include zero point librational amplitude because the reference spectra for which the $\langle\beta_o^2\rangle$ values were obtained contain the zero point librational motion. As a second model, it may be that $\langle\beta_o^2\rangle$ is governed by stochastic processes similar to those that drive diffusion in the solvent. One might expect that the temperature dependence of $\langle\beta_o^2\rangle$ would correlate with that of the viscosity of the buffer solution, $\eta_w(T)$, even though $\langle\beta_o^2\rangle$ is an equilibrium property and $\eta_w(T)$ is a transport property of the system. The solid line in Fig. 10 is a plot of $1/\eta_w(T)$ multiplied by a scaling factor versus temperature (see legend for details). The extension of this model (*dotted line*) to low temperatures shows that the limiting value of $\langle\beta_o^2\rangle$ is 0.0 ± 0.001 radians. Both of these models are in excellent agreement with the experimental data for $\langle\beta_o^2\rangle$, and suggest that the **A** and **g** tensors are independent of DNA motion.

Figure 11 shows the comparison of $\langle\beta_i^2\rangle$ versus $N + 1$ for the middle-labeled-T* DNA and the middle-labeled-Q DNA at $T = 0$°C. The slope of the $\langle\beta_i^2\rangle$ versus $N + 1$ curve for the T*-labeled DNA at 0°C (*solid line*) is approximately 0.6 times as steep as the slope for the Q-labeled DNA at 0°C (*solid line*), suggesting that the bending force constant for T* is 1.6 times larger than for Q; $\kappa = 2.53 \times 10^{-11} \pm 0.41 \times 10^{-11}$ ergs/rad^2 for T*- and $\kappa = 1.61 \times 10^{-11} \pm 0.08 \times 10^{-11}$ ergs/rad^2 for Q-labeled DNA. If we neglect the T* 96-mer data at 0°C, κ becomes $\kappa = 1.65 \times 10^{-11} \pm 0.40 \times 10^{-11}$ ergs/rad^2 (*dashed-dotted line*), essentially the same value as Q. The possible origin of the κ value differences for T* and Q will be considered in the Discussion section.

The analysis of $\langle\beta_i^2\rangle$ in Figs. 7–11 neglects the effects of torsional motion entirely. We showed in Eq. 13 how the effects of twisting could be included to give the overall tensorial averaging. For purposes of assessing the effects of twisting, we assume $\langle\beta_o^2\rangle = 0$ and, in Fig. 12, compare the two methods of averaging the tensors. The order parameter, S_i, of Eq. 9 is shown as a function of $\langle\beta_i^2\rangle$ for two preaveraging models. Method 1 is the standard method applying Eq. 10 which averages over two bending angles, and the spin system is aligned with the helix axis. Method 2 uses Eq. 14 and assumes that the spin probe is tilted by 20° and is averaged by $\langle\phi_i^2\rangle$ about the *z*-axis and $\langle\eta_i^2\rangle$ about *x* and *y*. For a given $\langle\beta_i^2\rangle$, method 2 reduces S_i more because it includes the twisting. The $\langle\beta_i^2\rangle$ used in the original method (method 1) multiplied by 0.9 give the same values of S_i found for method 2 (see Fig. 12), hence, any $\langle\beta_i^2\rangle$, or more precisely $2\langle\eta_i^2\rangle$ estimated by method 1, can be corrected for twisting by multiplying that estimate by 0.9. In essence, the $\langle\beta_i^2\rangle$ values reported are not due entirely to bending, but contain about a 10% contribution due to the twisting about the DNA helical axis.

The temperature dependence of the amplitudes of internal motion

Wilcoxon and Schurr (1983) examined the nature of the potential governing the interaction of adjacent base pairs. They found that, if the potential were a square well, then P_{db} would be independent of temperature, whereas if the potential were harmonic, then P_{db} would be inversely propor-

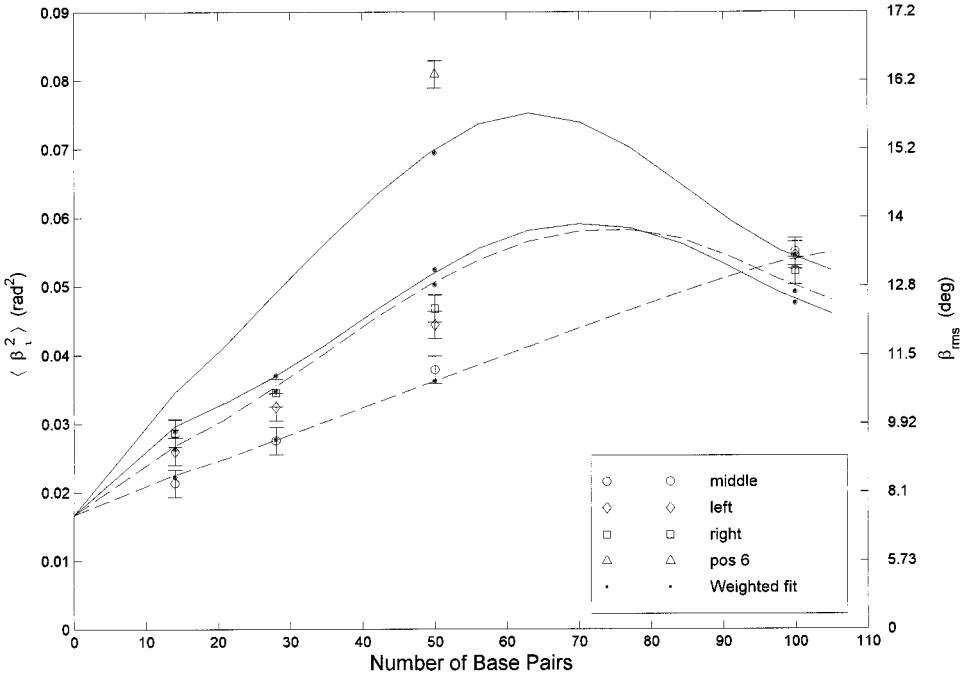

FIGURE 7 The mean squared oscillation parameter $\langle\beta_i^2\rangle$, due to the internal dynamics of DNA as a function of $N + 1$ base pairs of duplex DNA labeled on the right (□) ($i \approx \frac{3}{4}N$), the middle (○) ($i \approx \frac{1}{2}N$), and the left (◇) ($i \approx \frac{1}{4}N$), and a 50-mer labeled at position 6 (△) $i \approx \frac{1}{10}N$ all at $T = 0$°C, including the weighting of Eq. 16 (*dots*). The data are modeled using Eqs. 10 and 15, assuming a single $\langle\beta_o^2\rangle$, τ_o, and κ for all four spin-label positions, $\kappa = 1.61 \cdot 10^{-11}$ erg/rad^2, $\tau_o = 2.2 \times 10^{-10}$ sec, and $\langle\beta_o^2\rangle = 0.0167$ rad^2 at 0°C. The standard error to the fit is $\sigma = 3.3 \times 10^{-3}$. The τ_l are calculated according to Eqs. 7 and A17. A best-fit of the model to the data allows optimization of all three parameters, and they are $\tau_o = (1.97 \pm 0.29) \cdot 10^{-10}$ sec, $\kappa = (1.83 \pm 0.12) \cdot 10^{-11}$ erg/rad^2, and $\langle\beta_o^2\rangle = 0.0174 \pm 0.0012$ rad^2 ($\sigma = 1.88 \times 10^{-3}$). This optimized fit decreases the original χ^2 by a factor of 3. The weighted fits drawn through the data (dashed lines for the middle- and left-labeled DNAs and solid lines for the right- and 6-position-labeled DNAs) are only a visual guide using approximate i/N values to come close to the theory (*dots*).

tional to temperature. The theory of Eq. 3 predicts that, for a temperature-independent κ, the proportional (to temperature) model would describe a harmonic well, and a temperature-independent model would describe a square well. $\{\langle\beta_i^2\rangle - \langle\beta_o^2\rangle\}$, as a function of temperature, should behave in the same way as $2\langle\eta_i^2\rangle$ in Eq. 3, because these are the experimental data corresponding to $2\langle\eta_i^2\rangle$.

Figure 13 shows the difference quantity $\{\langle\beta_i^2\rangle - \langle\beta_o^2\rangle\}$ as a function of temperature for the 50-mer DNAs. The data were fit to a temperature-dependent and a temperature-independent model, as suggested above. Table 7 shows the fits of these models to the data with their errors. The lines in Fig. 13 depict a proportional model, $\langle\eta_i^2\rangle = m'T$, for the left-, middle-, and right-labeled DNAs. The temperature-independent model is a poorer model for these data than is the proportional one, despite the scatter in the data points. From the values of $f(i, N)$ in Table 4, Eq. 3 would predict that the ratio of slopes of the left- and right-labeled DNA data to that of the middle-labeled DNA data should be in the range from 1.8 to 1.9, which compares favorably to the experimentally determined value of 1.8 ± 0.1 (see Table 4). Eq. 3 predicts that the slope for the middle-labeled DNA should be $0.77 \cdot 10^{-4}$ rad^2/K, which also compares favorably with the fitted value of $(0.75 \pm 0.02) \cdot 10^{-4}$ rad^2/K in Table 7.

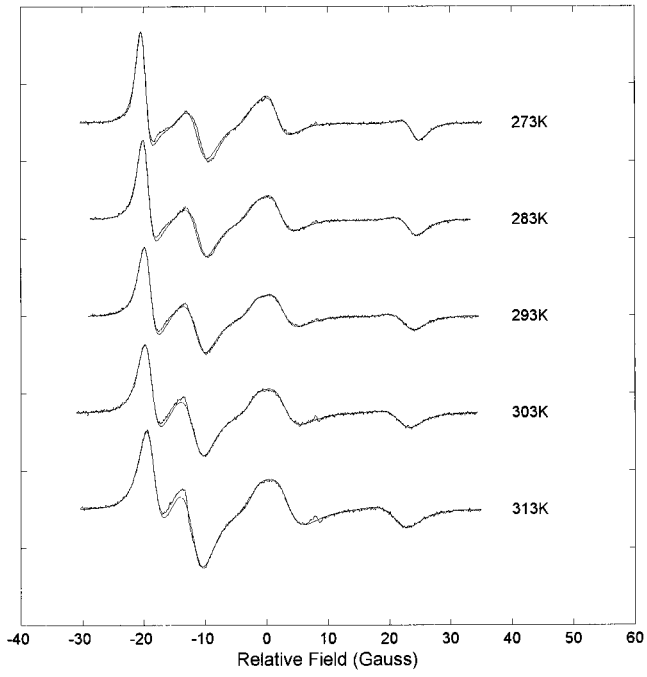

FIGURE 8 Q[^{15}N,D$_{12}$] middle-labeled 28-mer duplex DNA from 0 to 40°C CW-EPR data overlaid with simulations. N.B. Spectral width decreases with increased internal dynamics. Homogeneous linewidths and $\langle\beta_i^2\rangle$ (Fig. 9) were obtained by optimizing the best-fit simulations to the spectra.

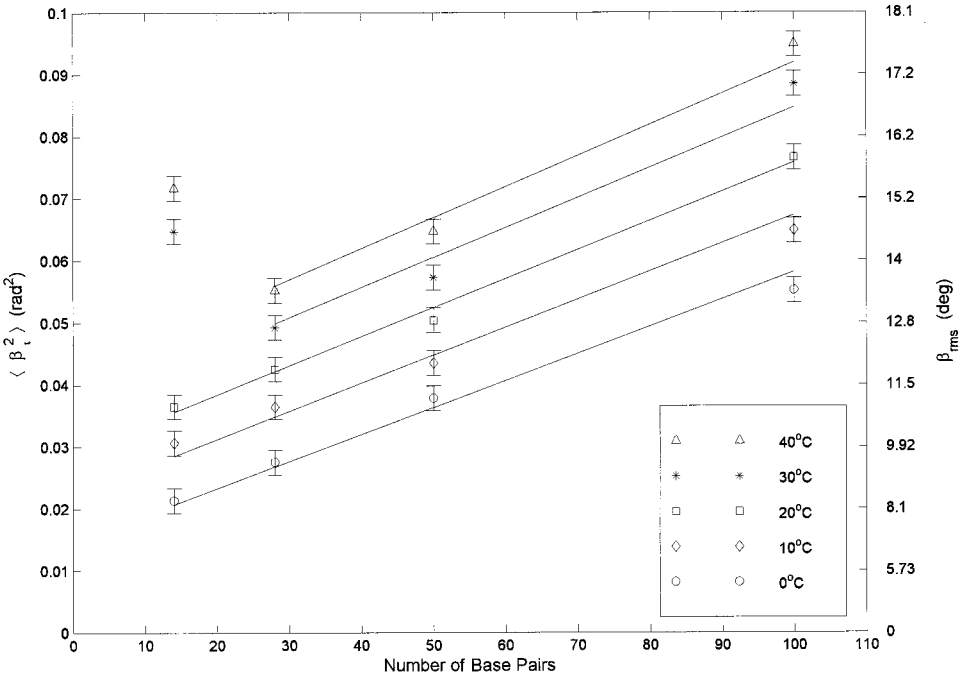

FIGURE 9 The mean squared oscillation parameter $\langle\beta_i^2\rangle$, due to the internal dynamics of DNA is plotted as a function of the $N + 1$ base pairs of duplex DNA for middle-labeled ($i \approx \frac{1}{2}N$) DNA at $T = 0°$ (○), 10° (◇), 20° (□), 30° (*), and 40°C (△). The data are least-squares fit to the model $\langle\beta_i^2\rangle = [(N + 1)k_BT/6\kappa] \cdot f(i, N) + \langle\beta_o^2\rangle$, assuming a single, temperature-independent, force constant, $\kappa = (1.44 \pm 0.04) \cdot 10^{-11}$ ergs/rad^2. The data, when analyzed at each of the five temperatures, gave the following:

Temperature (°C)	Slope $\pm$ $\sigma \cdot 10^4$ (rad^2/bp)	$k \pm \sigma_\kappa \cdot 10^{11}$ (ergs/rad^2)	$\langle\beta_o^2\rangle \pm \sigma$ (rad^2)
0	3.92 ± 0.20	1.61 ± 0.08	0.015 ± 0.001
10	3.96 ± 0.14	1.64 ± 0.06	0.022 ± 0.001
20	4.68 ± 0.26	1.44 ± 0.04	0.029 ± 0.001
30	5.60 ± 0.60	1.24 ± 0.14	0.036 ± 0.001
40	5.60 ± 0.40	1.29 ± 0.08	0.042 ± 0.001

DISCUSSION

The effects of the bending relaxation times of the internal collective motional modes of motion must be included in the calculation of internal dynamics. These effects are consistent with the apparent falloff of $\langle\beta_i^2\rangle$ with increasing length for the distally labeled DNAs (Fig. 7). The relaxation times were not measured but calculated from theory; nevertheless, the agreement with data indirectly confirms that the calculated correlation times are of the correct order of magnitude. In particular, the time scale for the longest internal mode is confirmed by the absence of a falloff of $\langle\beta_i^2\rangle$ as a function of duplex length for the middle-labeled DNA, implying that this longest mode does not contribute to the rotational relaxation for middle-labeled DNA. The weakly bending rod model works very well to qualitatively explain the position dependence of $\langle\beta_i^2\rangle$ in duplex DNA.

Within the framework of the weakly bending model, we can now begin to consider data that heretofore seemed anomalous. The higher temperature 14-mer duplex DNA data of Fig. 9 are left out of the pooled fit because of the large and unexplained deviation from the trend above 20°C. The 14-mers are susceptible to concentration effects (stacking) at low temperatures and produce depressed $\langle\beta_i^2\rangle$ values (we used very low concentrations to avoid such effects, <1 mg/ml). We suggest that the 14-mers may be susceptible to a structural transition around 25°C that was not detected by either circular dichroism (CD) or a ultra violet (UV)/Vis monitored melting curve. CD and UV temperature studies (performed under the same concentration and buffer conditions as the EPR experiments) of these very 14-mer duplexes gave no indication of any such structural changes (data not shown). To test whether there could be a structural rearrangement of the labeled base pair relative to the helix axis to give large $\langle\beta_i^2\rangle$ values, we fixed $\langle\beta_i^2\rangle$ in the lineshape analysis for the 14-mer duplex at 30 and 40°C, appropriate to their theoretical $\langle\beta_i^2\rangle$ values, and allowed the tilt angle to optimize the fits. The simulations for the high temperature data best-fit the theorized $\langle\beta_i^2\rangle$ values when the tilt angle, θ_{tilt}, was increased from 20° to 27°. Therefore, one possible explanation for the $\langle\beta_i^2\rangle$ values of the 14-mers at high temperature could be an increase in the tilt angle of the probe in these samples.

In addition to large $\langle\beta_i^2\rangle$ values for the 14-mers, the left- and right-labeled 50-mers show different dynamics (Fig. 13) as well above 25°C. It is quite possible that the higher temperature data for these 50-mers analyzed at a larger tilt

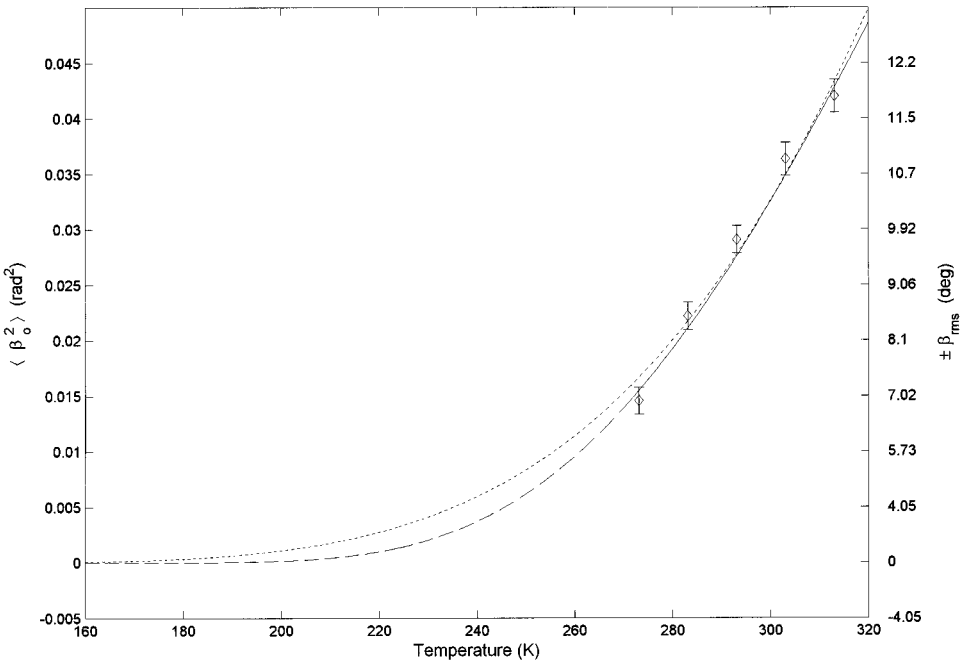

FIGURE 10 The values of the mean squared oscillation parameter $\langle\beta_o^2\rangle$ as a function of temperature, T, in Kelvin (◇). Superimposed is the plot of $(k_B\theta/\kappa_{hw})\{e^{-\theta/T}/(1-e^{-\theta/T})\}$, which is the functional form for libration in a harmonic well, shown as the dotted line. k_B is Boltzmann's constant, $\theta = (2040 \pm 150)K$ is the Debye temperature and $\kappa_{hw} = (2.0 \pm 0.8) \cdot 10^{-11}$ ergs/rad^2 is the force constant for the harmonic well. Superimposed is $2.8 \cdot \eta_w^{-1}(T)$ shown as the solid line. $\eta_w(T)$ is the viscosity of water in poise. The dashed line is based on a calculation of $\eta_w(T)$ below the freezing point of water, assuming the same functional form above −10°C, in an attempt to predict the rigid limit behavior for $\langle\beta_o^2\rangle$.

angle (~27°) would also yield decreased $\langle\beta_i^2\rangle$ values. Because there are no independent data to support a structural rearrangement, it seems premature to investigate this further quantitatively. The above are two different examples that suggest a structural rearrangement between 20 and 30°C.

We now consider whether the bending potential is better described as a harmonic or square well. The temperature dependence of $\langle\eta_i^2\rangle$ (examined via $\{\langle\beta_i^2\rangle - \langle\beta_o^2\rangle\}$ in Fig. 13) indicates whether the interactions of adjacent base pairs are governed by a square or harmonic potential. If the potential surface in which the r.m.s. excursions occur were a square well, and if the force constant were independent of temperature, then $\langle\eta_i^2\rangle$ would be temperature independent. If the potential surface were harmonic, then $\langle\eta_i^2\rangle$ should be proportional to the temperature. In fitting the harmonic model to the data we find that the slope for the left-, right-, and middle-labeled 50-mers of DNA are consistent with the same quantities measured by fitting $\langle\beta_i^2\rangle$ as a function of length shown in Figs. 5 and 7. The fit to the proportional model is significantly better than the fit to the temperature-independent model because the standard error for the proportional model is half that of the standard error for the

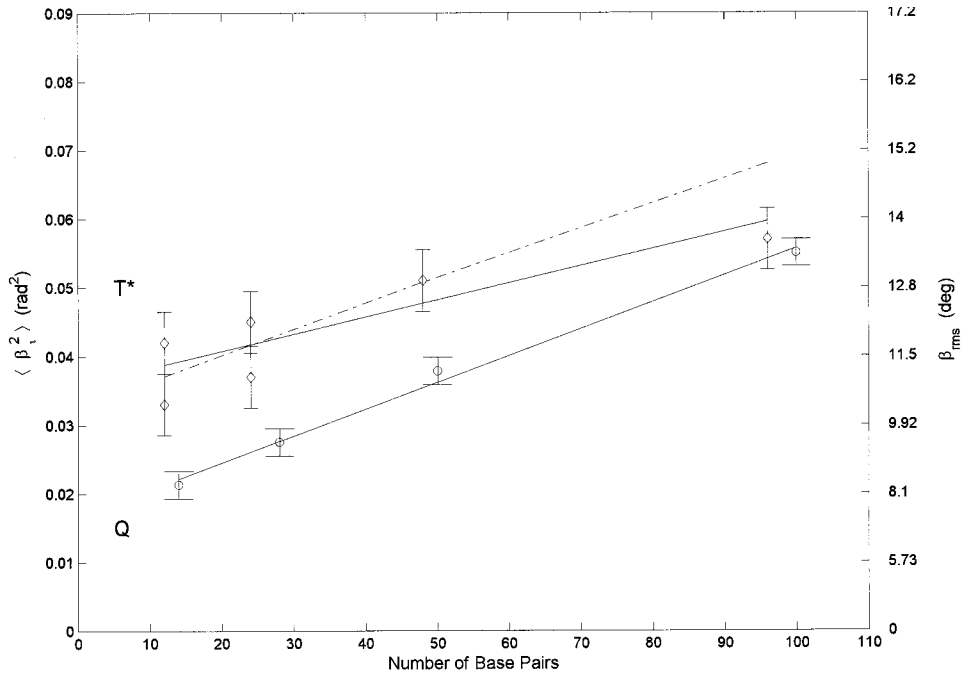

FIGURE 11 Comparison of the mean squared oscillation parameter $\langle\beta_i^2\rangle$ for T* (◇) and Q (○), both middle-labeled DNA as a function of length, $N + 1$. Solid line for Q data shows calculated $\langle\beta_i^2\rangle$ for 0°C data ($\kappa = 1.61 \times 10^{-11} \pm 0.08 \times 10^{-11}$ ergs/rad^2). Solid line for T* shows calculated $\langle\beta_i^2\rangle$ for 0°C data ($\kappa = 2.53 \times 10^{-11} \pm 0.41 \times 10^{-11}$ ergs/rad^2). Dashed-dotted line for T* shows calculated $\langle\beta_i^2\rangle$ for the 12-, 24-, and 48-mer 0°C data neglecting the 96-mer data point ($\kappa = 1.65 \times 10^{-11} \pm 0.40 \times 10^{-11}$ ergs/rad^2). The value of every individual $\langle\beta_i^2\rangle$ is smaller for Q- than for T*-labeled DNA.

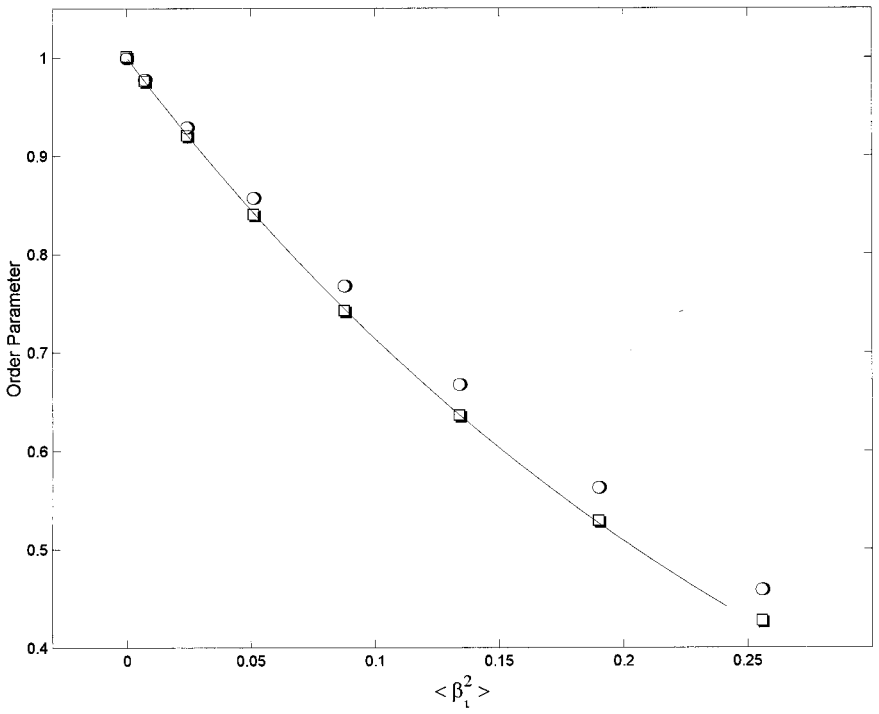

FIGURE 12 The order parameter, S_i, calculated by method 1, Eq. 10 (○) and by method 2, Eq. 14 (□) as a function of the mean squared oscillation parameter $\langle\beta_i^2\rangle$ (see text and Eq. 13). The solid line is the order parameter calculated by method 1 with the values of $\langle\beta_i^2\rangle$ multiplied by 0.9.

temperature-independent model. Thus, the data suggest that the potential surface is characterized better as harmonic than square well. Additionally, κ may itself have a weak temperature dependence (Schurr et al. 1992). The data in Figs. 9 (see legend) and 13 are suggestive of a change in κ above 20–25°C. The apparent change in κ above 20°C may reflect either a true change in the bending potential, or a structural change in which the tilt angle of the probe is increased. Therefore, we do not report a P_{db} associated with the data in this temperature range.

The low temperature (0–10°C) data for the middle-labeled DNAs in Fig. 9 were analyzed to give a κ value of $(1.62 \pm 0.05) \cdot 10^{-11}$ ergs/rad^2. The fit to the $\langle\beta_i^2\rangle$ values for the left-, middle-, and right-labeled DNAs at 0°C in Fig. 7 were also consistent with this κ value, which was obtained from Figs. 5 and 9. When the $\langle\beta_i^2\rangle$ in Fig. 7 were analyzed

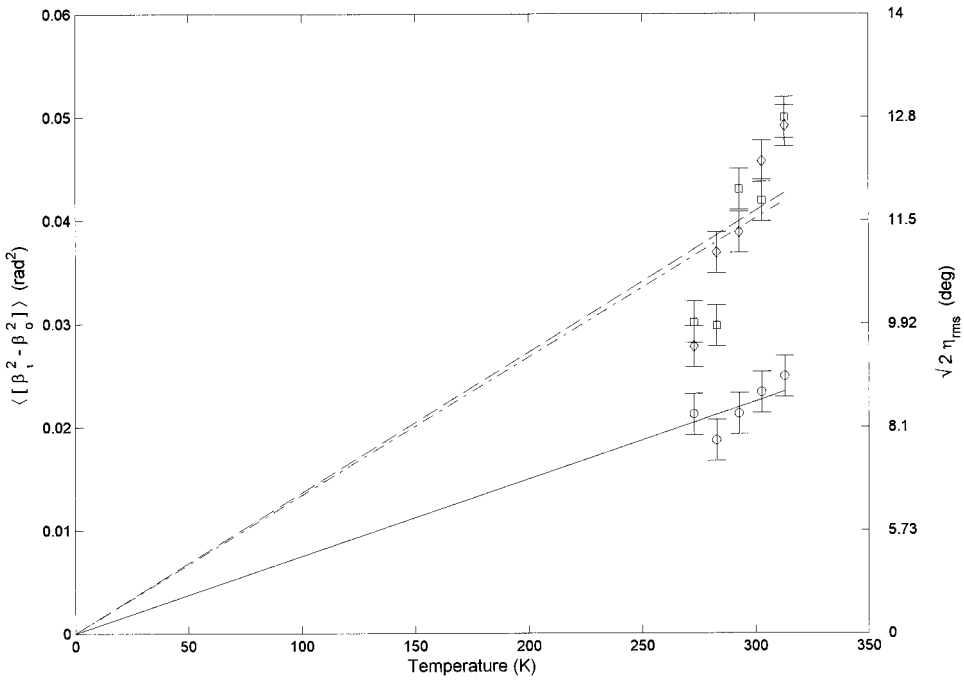

FIGURE 13 The quantity $\{\langle\beta_i^2\rangle - \langle\beta_o^2\rangle\}$ is plotted as a function of temperature for the 50-mer DNAs. The values of $\{\langle\beta_i^2\rangle - \langle\beta_o^2\rangle\}$ are from the right- (□), middle- (○), and left- (◇) labeled 50-mers. The lines are proportional least-squares fits to the data. The solid line is for the middle-labeled 50-mer, the short dashed line is for the left-labeled 50-mer and the long dashed line is for the right-labeled 50-mer. Slopes, intercepts, and standard errors of fit for these models are given in Table 7.

TABLE 7 Slopes and intercepts of the temperature analyses of $\{\langle\beta_i^2\rangle - \langle\beta_o^2\rangle\}$

Model	Data Sets Fit to Models	Intercept (rad^2)	Slope (rad^2/K)	Standard Error (rad^2) $\times 10^3$
Proportional to T	Left-right label	—	$(1.4 \pm 0.1) \times 10^{-4}$	5.8
	Middle label	—	$(0.75 \pm 0.02) \times 10^{-4}$	1.4
Independent of T	Left-right label	0.039 ± 0.004	—	8.5
	Middle label	0.022 ± 0.001	—	2.4

by a best-fit model in which κ, $\langle\beta_o^2\rangle$, and τ_o were all optimized, the value of κ increased by less than 15%. The value of $\langle\beta_o^2\rangle$ and τ_o changed by 5 and 10%, respectively. These differences are on the order of the uncertainty in each of the parameters, which is also calculated from the fitting. If the differences in the values of κ are considered to be significant, then one might consider the consequences. It is possible that there may be a greater stiffness, or a larger bending force constant, in the more distal regions of linear duplex DNA, and such features are not treated adequately in the simple weakly bending rod theory. The estimate for κ must be taken to be in the range of $(1.62 \pm 0.05) \cdot 10^{-11}$ ergs/rad^2 when considering only the middle-labeled bases, and in the range of $(1.83 \pm 0.12) \cdot 10^{-11}$ ergs/rad^2 when considering all labeled positions. These two ranges somewhat overlap one another.

The inclusion of the internal collective twisting motions reduces the contribution of flexure by 10%, and increases the best-fit value of the bending force constant (and thereby P_{db}) by 10% (Fig. 12). The best estimate for the dynamic bending persistence length, P_{db} (reported to 2σ), obtained from the middle-labeled data, is thus 1500 ± 100 Å at 20°C. Similarly, the estimate obtained from fitting all the labeled positions simultaneously, when corrected also for the twisting dynamics, gives a value of 1700 ± 200 Å at 20°C. The persistence lengths that we have measured relate primarily to the dynamic flexural component of the persistence length, for dynamic processes occurring on the submicrosecond time scale. Permanent bends have almost no impact on this estimate, and would only alter the analysis by slightly changing the diffusion coefficients as estimated by the theory of Tirado and Garcia de la Torre (1980). Computations done in our laboratory indicate that a permanent bend on the order of 5° per base pair, variously phased, would change the diffusion coefficients by a negligible amount. The relative tilt angle of the base to the mean helix axis could be changed by a few degrees, but not enough to markedly alter the results presented herein (Okonogi et al., 1997).

The length-independent motion of the probe scales with solvent viscosity (Fig. 10) and has a $7° \pm 1°$ r.m.s. oscillation amplitude in each of the two directions perpendicular to the helix axis, at 20°C. These estimates are for DNA in 0% w/v sucrose in PNE at 20°C and compare well with the current estimate of 7–10° r.m.s. oscillation amplitude using an ethidium probe intercalated into duplex DNA (Shibata et al., 1985; Wilcoxon and Schurr, 1983). The extrapolation of $\langle\beta_o^2\rangle$ to zero (*dashed line*) in Fig. 10 predicts no internal amplitudes of motion at low temperatures and suggests that our tensors were well chosen. The **g** and **A** tensors were optimally fit using a combination of EPR frequencies. As illustrated in Fig. 3, **g** tensors are best found at high frequency (94 GHz) and **A** tensors are more prominent at low frequency (9.4 GHz). The spectra at both frequencies are well accounted for by nondynamics simulations with a single set of **A** and **g** tensors. The tensors were then adjusted according to Eq. 8 to account for the residual motion of $\langle\beta_i^2\rangle = 0.012$ rad^2 and are reported in Table 6.

These experiments extend testing of the weakly bending rod theory beyond previous studies. Hustedt et al. (1993a) asked whether the values of $\langle\beta_i^2\rangle$ would increase linearly with DNA duplex length for a centrally labeled base pair. It was shown that $\langle\beta_i^2\rangle$ did increase linearly with duplex length using the T* probe (see Fig. 2), giving a P_{db} of 2500 ± 700 Å at 20°C. Here, we examined whether $\langle\beta_i^2\rangle$ would follow the same trend as a function of length and label position with the spin probe Q. Both labels give good agreement between the experimental results and the predictions of theory, in that both demonstrate a linear relation between $\langle\beta_i^2\rangle$ and $(N + 1)$. However, the estimates of P_{db} using the spin probe Q are only about 0.60–0.68 times the earlier estimates obtained using the T* probe (see Fig. 11). When considering why such differences might exist, one should consider three aspects: 1) the two probes may not necessarily be expected to give the same dynamic persistence lengths because the optimum P_{db} values may not be completely independent of the probe; 2) a 1.47–1.66-fold difference in persistence lengths needs to be considered in the context of the reported errors, and relative to the total persistence length; and 3) the probes are measuring different DNAs.

We do not necessarily expect the Q probe and the T* probe to report the same persistence length using the same model of DNA motion in the analysis. The unknown distribution of orientations and unknown local angular motions of the T* probe relative to the DNA differ significantly from those for the Q probe as a result of design, and may alter the dynamics reported accordingly. Although T* is better than many other probes used now and in the past because of its relatively high-order parameter, it is still considered a "floppy" probe with its remaining one degree of freedom. The data using Q may be more reliable in that Q has no degrees of freedom independent of the base. The length-independent amplitude of motion of T* is governed by the

size of the pocket around it that is created by neighboring base pairs winding in the helix. This point was demonstrated in a previous paper (Hustedt et al., 1995). Examination of Fig. 11 (0°C data) shows that the slopes of $\langle\beta_i^2\rangle$ versus $N + 1$ for the Q- and T*-labeled DNAs are very similar up to the 96-mer and 100-mer bp data points. If the length-independent contribution for the 96-mer were increased by 0.012 rad^2, then the slopes are identical. Secondary structural changes, either local to the probe or global, may be occurring as the DNA gets longer. Hence, the pocket surrounding the T* probe may be restricting the length-independent motion of T* and lowering the overall dynamics reported in the $\langle\beta_i^2\rangle$ value. Q is not expected to have this problem because it is rigidly fused to the base, and a subtle change in the groove dimensions would not affect the length-independent contribution to the overall dynamics.

The 1.47–1.66-fold difference between the pooled T* value of 2500 ± 700 Å and the final Q value of 1500 ± 100 Å is not as significant as it may seem. The difference of 1000 Å between the two P_{db} values is only about 1.2 times the sum of their standard deviations. Equally relevant are the percentages of the total inverse persistence length that these two estimates account for. If P_t is 500 Å, then the estimated contribution to the total inverse persistence length from the P_{db} of Q is 33 ± 3% and from the P_{db} of T* is 20 ± 7%. Both percentages lie in the range of 30% of the total inverse persistence length, representing rather similar percentages of the P_t.

The sequences of DNA used in the two experiments were quite different. In particular, there are AT-base pair rich regions in the vicinity of the T* probe that are not found in the vicinity of the Q probe. The longer T*-containing sequences are more GC-base pair rich. If AT sequences are more flexible than GC, then this tends to enhance the dynamics of the short pieces of T*-containing DNA relative to that of the longer T*-containing DNAs. Therefore, the slope of the line of mean square amplitude as a function of length would tend to be less for the T*-containing DNA. Hence, AT-rich regions near the probe could account for some of the differences seen. The model used in analyzing the data herein does not account for different dynamics due to different base pair sequences. This is a limitation of the model; however, future work will expound on the sequence dependence of dynamics. There are marked differences in the flexibility of AT and GC repeats (Okonogi et al., 1997).

The presence of an A-T* base pair increases the T_m for an 11-mer duplex DNA by less than one degree. It has been suggested by others (Strobel et al., 1995) that such a rise in T_m indicated a change in the flexibility, i.e., stiffening of the molecule, due to the presence of the A-T* pair. The presence of Q and its base pair, 2AP, actually decreases the T_m of an 11-mer duplex DNA by about 7 degrees (Miller et al., 1995). By the same reasoning, the molecule should become more flexible by the presence of the 2AP-Q pair. We do measure a smaller persistence length, but all the $\langle\beta_i^2\rangle$ values for the Q probe are much less than for the probe T*, indicating a higher order parameter and a more tightly coupled probe. Thus, these data show an inverse correlation between T_m and dynamics. The T_m of melting refers to a state of transition to separate strands, whereas dynamics is motion limited to a well near a local potential minimum. The dynamics observed by the present experiments reflect excursions within the potential well of the 10.4 base pairs per turn B-form DNA. The B-form nature of the duplex DNA is confirmed by CD of the 14-mer duplex DNA in the standard PNE buffer from 0 to 60°C (T_m) to 75°C (full melt, data not shown) and 2D-NMR data (Alley, 1996). All EPR data presented here are acquired between 0 and 40°C, well below the onset of melting (about 50°C for the 14-mers). It would be obvious in the EPR spectra if there were any single stranded DNA present (in slow exchange with the sample), because EPR experiments are very sensitive (as low as 1% sensitivity) to rapidly reorienting spins.

CONCLUSIONS

We suggest that the total persistence length, P_t, is the sum of three components (Schurr et al., 1997): $1/P_t = 1/P_s + 1/P_{db} + 1/P_{srs}$. The Schellman–Harvey estimate for the static contribution to the persistence length, P_s, is sequence dependent and ranges from ~1370 to ~2000 Å. Assuming the dynamic estimate developed herein, $P_{db} \sim 1500$–1700 Å, the Schellman–Harvey static estimate, and the literature $P_t \sim 500$ Å, we estimate $P_{srs} \sim 1500$ Å and that slowly relaxing structures play an important part in defining the overall persistence length. In short, each of the three terms contributes about one-third to the total persistence length.

The novelty of these short-time dynamic persistence length measurements implies that practically nothing is known about its dependence on the sequence, the position of the label, or the length of the DNA. We have shown that the quantity $\langle\beta_i^2\rangle$ that we measure does match the simple theory in several important ways: 1) there is a linear relation between our measured $\langle\beta_i^2\rangle$ and the length of the DNA; 2) our measured $\langle\beta_i^2\rangle$ does increase as the probe is placed further from the middle of the DNA, in very good quantitative agreement with the predictions of the theory; 3) the theory, as adapted for our EPR experiment, predicts that the apparent mean squared amplitudes will vary with DNA length in a nonlinear manner due to the time scale of the internal bending modes; and 4) the increase in the measured $\langle\beta_i^2\rangle$ values as a function of increasing temperature follows the predictions of the theory with no new adjustable parameters. Thus, the quantity we measure does bear a strong resemblance to the mean square amplitude of motion as predicted by the weakly bending rod theory. We do not discuss the effects of sequence in this paper, but the results of extensive experiments on the effects of sequence to modulate the dynamic bending rigidity have been performed, and will be presented elsewhere.

APPENDIX

We now give a more complete account of the application of the elegant theory of the weakly bending rod model developed by Schurr and coworkers (Schurr et al., 1992; Song et al., 1990; Wu et al., 1987) to describe the effects of dynamics on linear CW-EPR spectra. Mathematically, DNA is treated as a flexible rod-shaped object and, although duplex DNA may be curved over a long distance scale, mean local cylindrical symmetry is assumed to occur about each base. This symmetry arises from the helical nature of duplex DNA: each base is connected to its neighbor by bonds that act as Hookean springs that resist both twisting and bending. The discussion of rotational dynamics is in terms of displacements about a body fixed-axis system coincident with the DNA molecule in its canonical form. The principal axis is taken to be the *z*-axis, which is coincident with the local helix axis. The mean squared displacement about the *z*-axis, $\langle\Delta_z(t)^2\rangle$, corresponds to the twisting of DNA, whereas $\langle\Delta_x(t)^2\rangle$ and $\langle\Delta_y(t)^2\rangle$, the mean squared displacements about *x* and *y*, correspond to the bending of DNA. The mean local cylindrical symmetry of the DNA allows the simplifying assumption that the mean squared displacements about *x* and *y* are the same and $\langle\Delta_x(t)^2\rangle = \langle\Delta_y(t)^2\rangle$. Moreover, the rotations in the three different directions are taken to be driven by statistically independent processes, and thus, cross terms in the displacements, such as $\langle\Delta_x(t)\Delta_y(t)\rangle$, vanish. The displacements include all modes of motion: the length-independent modes (motion of the spin probe or the base pair independent of the DNA to which it is attached); the internal collective modes (dynamics at one point of the molecule as a consequence of motions from the rest of the molecule); and the uniform modes (overall tumbling of the molecule as a rigid body). This model forms the basis for our discussion of how an idealized piece of duplex DNA may relax: it is very simple and has few adjustable parameters.

If DNA had no internal motion but tumbled with uniform motion as a rigid cylinder, then $\frac{1}{2}\langle\Delta_x(t)^2\rangle = D_\perp t$ and $\frac{1}{2}\langle\Delta_z(t)^2\rangle = D_\parallel t$, where $D_\parallel$ and $D_\perp$ are the rotational diffusion coefficients for the motion about the helix axis and perpendicular to it, respectively. However, both the internal collective and uniform motional modes contribute to the displacements, and therefore, with internal rotational motion about the *z* or helix axis defined by ϕ and rotation perpendicular to *z* defined by η and θ, the angular displacements for a probe at the *i*th base pair are given by

$$\begin{aligned}
\tfrac{1}{2}\langle\Delta_x(t)^2\rangle &= D_\perp t + \langle[\eta_i(t) - \eta_i(0)]^2\rangle,\\
\tfrac{1}{2}\langle\Delta_y(t)^2\rangle &= D_\perp t + \langle[\theta_i(t) - \theta_i(0)]^2\rangle,\\
\tfrac{1}{2}\langle\Delta_z(t)^2\rangle &= D_\parallel t + \langle[\phi_i(t) - \phi_i(0)]^2\rangle.
\end{aligned} \tag{A1}$$

We assume that there is a single bending and a single twisting force constant between base pairs, and that each is independent of base pair sequence. The mean squared amplitudes of displacement for both twisting, $\langle\Delta_z(t)^2\rangle$, and bending, $\langle\Delta_x(t)^2\rangle$, are calculated from equilibrium statistical mechanics. The potential energy that confines the oscillators is harmonic in the angular displacement (Schurr, 1976; Wu et al., 1987). The twist energy of a single oscillator is $U = \frac{1}{2}\phi\alpha\phi$, where α is the twisting force constant. For a single oscillator, the total mean squared amplitude of the displacement from the origin is given by the equilibrium distribution,

$$\begin{aligned}
\langle\phi(\infty)\phi^t(\infty)\rangle &= \int_{-\infty}^{\infty}\phi P(\phi)\phi\,\mathrm{d}\phi\\
&= \int_{-\infty}^{\infty}\phi^2\frac{\exp\{-U/k_BT\}}{\int\exp\{-U/k_BT\}\,\mathrm{d}\phi}\,\mathrm{d}\phi\\
&= \int_{-\infty}^{\infty}\phi^2\frac{\exp\{-\alpha\phi^2/2k_BT\}}{\sqrt{2\pi k_BT/\alpha}}\,\mathrm{d}\phi = \frac{k_BT}{\alpha},
\end{aligned} \tag{A2}$$

where k_B is Boltzmann's constant, and *T* is the temperature in Kelvin.

For an ensemble of $(N+1)$-coupled oscillators with nearest neighbor interactions, the analogous problem is written in terms of a vector of angular displacements, $\vec{\phi}$, and the $N+1$ by $N+1$ matrix **A**,

$$\vec{\phi} = \begin{pmatrix}\phi_1\\ \phi_2\\ \vdots\\ \phi_{N+1}\end{pmatrix}$$

and

$$A = \begin{pmatrix}
1 & -1 & 0 & \cdots & & 0\\
-1 & 2 & -1 & & & \vdots\\
0 & -1 & 2 & & & \\
\vdots & 0 & -1 & & & \\
 & & & & 2 & -1\\
0 & \cdots & & & -1 & 1
\end{pmatrix}. \tag{A3}$$

The potential energy is $U = \frac{1}{2}\alpha\vec{\phi}^tA\vec{\phi}$. Diagonalizing the $(N+1)\times(N+1)$ matrix **A** yields the $N+1$ eigenvalues Λ and the $(N+1)\times(N+1)$ matrix of eigenvectors **Q**: $Q^tAQ = \Lambda$. Each eigenvalue and eigenvector corresponds to a motional mode; all the eigenvalues are non-negative. Defining the normal modes' coordinates $\vec{\rho} = Q^t\vec{\phi}$ results in $U = \frac{1}{2}\alpha\vec{\rho}^t\Lambda\vec{\rho}$ and the equilibrium average becomes

$$\begin{aligned}
\langle\vec{\phi}(\infty)\vec{\phi}^t(\infty)\rangle &= \int_{-\infty}^{\infty}\vec{\phi}P(\phi)\vec{\phi}^t\,\mathrm{d}\phi^N\\
&= Q\int_{-\infty}^{\infty}\vec{\rho}\,\frac{\exp\{-U/k_BT\}}{\int\exp\{-U/k_BT\}\,\mathrm{d}\rho^N}\,\vec{\rho}^t\,\mathrm{d}\rho^NQ^t\\
&= \frac{k_BT}{\alpha}Q\Lambda^{-1}Q^t.
\end{aligned} \tag{A4a}$$

The lowest eigenvalue, $\lambda = 0$, corresponds to the uniform motion, which is treated separately. Therefore, to study only the internal motions, $\lambda = 0$ is removed from Λ^{-1} and the associated column vector is removed from **Q**. The resulting matrix $Q\Lambda^{-1}Q^t$ is also called the pseudoinverse of **A** (MathWorks, 1996).

A similar treatment has been developed for bending. There are two independent directions assumed to have the same bending force constant, κ, due to the mean local cylindrical symmetry. Therefore, the mean squared amplitudes in both directions are the same. The total bending potential energy is $U = \frac{1}{2}\kappa\vec{\eta}^tA\vec{\eta} + \frac{1}{2}\kappa\vec{\theta}^tA\vec{\theta}$. Because there are only *N* (not $N+1$) bending angular coordinates, $\vec{\eta}$ and $\vec{\theta}$ are vectors of length *N*, and **A** is an $N\times N$ matrix (Wu et al., 1987). By an argument similar to that given above,

$$\langle\vec{\eta}(\infty)\vec{\eta}^t(\infty)\rangle = \frac{k_BT}{\kappa}Q\Lambda^{-1}Q^t, \tag{A4b}$$

where Λ is an $(N-1)\times(N-1)$ matrix. The uniform mode of motion, for which the eigenvalue is zero, has been removed from Λ and from **Q**.

The time constants for the relaxation of the internal modes—needed later—can be obtained. The diffusion equation for twisting is most easily represented by the Langevin equation, which is similar to, and leads to the same type of solutions as, the Smolochowski diffusion equation (Robinson et al., 1980). We review the results for a single bead, then extend consideration to that of $N+1$ coupled beads. The quantity we seek is the mean square oscillation amplitude as a function of time. For a single particle in a restoring potential, $U = \frac{1}{2}\phi\alpha\phi$, the Langevin equation is a modified form of Newton's law: $J\ddot{\phi} + \gamma_t\dot{\phi} = F(\phi) + R(t)$, where $\gamma_t\dot{\phi}$ represents drag proportional to the friction factor γ_t and angular velocity $\dot{\phi}$; *J* is the

rotational inertia; $F(\phi) = -\mathrm{d}U/\mathrm{d}\phi = -\alpha\phi$ is the torque arising from the potential U; and $R(t)$ is the torque from the Brownian fluctuations of the solvent. When the confining potential is large compared to the inertial term, i.e., $F(\phi) > J\ddot{\phi}$, then the Langevin equation is approximately $\gamma_t\dot{\phi} + \alpha\phi = R(t)$.

The fluctuating torque, $R(t)$, (Forster, 1975; Schurr, 1976; Song et al., 1990) has a mean of zero, $\langle R(t)\rangle = 0$; and does not correlate with the libration of the particle, $\langle\phi(t')R(t)\rangle = 0$; and has mean squared statistical fluctuations so that $\langle R(t')R(t)\rangle = 2(k_BT/\gamma_t)\cdot\delta(t - t')$. Therefore, the Langevin equation for the average values of ϕ is simplified to $\gamma_t\langle\dot{\phi}\rangle + \alpha\langle\phi\rangle = 0$, and $\gamma_t(d\langle\phi(0)\phi(t)\rangle/\mathrm{d}t) + \alpha\langle\phi(0)\phi(t)\rangle = 0$. The solutions to these homogeneous differential equations are

$$\langle\phi(t)\rangle = \langle\phi(0)\rangle e^{\{-\alpha_l/\gamma_l\}}$$

and (A5)

$$\langle\phi(0)\phi(t)\rangle = \langle\phi(0)^2\rangle e^{\{-\alpha_l/\gamma_l\}}.$$

Because the distribution of angles is independent of time and is always at equilibrium, it follows that $\langle\phi(0)^2\rangle = \langle\phi(t)^2\rangle = k_BT/\alpha$. We will need the identity

$$\langle(\vec{\phi}(t) - \vec{\phi}(0))(\vec{\phi}(t) - \vec{\phi}(0))^t\rangle = 2\{\vec{\phi}(0)\vec{\phi}(0)^t\rangle - \langle\vec{\phi}(t)\vec{\phi}(0)^t\rangle\}.$$

The Langevin equation for the coupled torsional oscillators looks very similar to the above expression: $J\ddot{\vec{\phi}} + \gamma_t\dot{\vec{\phi}} + \alpha A\vec{\phi} = \vec{R}(t)$. Premultiplying by Q^t and substituting $\vec{\rho} = Q^t\vec{\phi}$ yields

$$J\ddot{\vec{\rho}} + \gamma_t\dot{\vec{\rho}} + \alpha\Lambda\vec{\rho} = Q^t\vec{R}(t), \quad \text{where} \quad Q^tAQ = \Lambda. \tag{A6}$$

Again, each of the normal modes is statistically independent of the others. Following the reasoning used for the single particle case in Eq. A5, the self, and cross, correlations of the mean squared oscillation amplitudes for the internal twisting motions become

$$\langle\vec{\phi}(t)\vec{\phi}^t(0)\rangle = \frac{k_BT}{\alpha}Q\Lambda^{-1}(\exp\{-\alpha\Lambda t/\gamma_t\})Q^t \tag{A7}$$

where $\mathbf{\Lambda}$ is the $N \times N$ eigenvalue matrix of $\mathbf{A}$, and $\mathbf{Q}$ is the $(N + 1) \times N$ eigenvector matrix, after the eigenvector and eigenvalue corresponding to the uniform motion ($\lambda = 0$) has been removed. By inspection of Eq. A7, the relaxation time for the lth internal mode is

$$\tau_{(\mathrm{twist})_l} = \gamma_t/\alpha\lambda_l. \tag{A8}$$

In analogy with the single bead case, the mean square correlation due to twisting is

$$\langle(\vec{\phi}(t) - \vec{\phi}(0))(\vec{\phi}(t) - \vec{\phi}(0))^t\rangle = 2\frac{k_BT}{\alpha}Q\Lambda^{-1}\left(1 - \exp\left\{-\Lambda\frac{\alpha t}{\gamma_t}\right\}\right)Q^t. \tag{A9}$$

From Eq. A9, it follows that the total mean squared amplitude is the sum of the amplitudes of each of the normal modes, and each mode builds to its equilibrium value as time goes to infinity. When Eq. A9 is evaluated at the infinite time limit, the same result as that for Eq. A4 is obtained.

The flexural motions, whose mathematical forms are similar to those for twisting, differ because the hydrodynamic interactions between the beads are large for flexural motions and therefore makes the Langevin equation more complicated. Song et al. (1990) have developed the problem for the case of $N_b + 1$ effective spherical beads. The displacement coordinate for each of the beads is η_i—the angle between the i and the $i + 1$ bead in the y direction: $\eta_i \approx \sin(\eta_i) = (y_{i+1} - y_i)/h_b$ or, in vector notation,

$$\vec{\eta} = \frac{1}{h_b}\delta\cdot\vec{y}.$$

h_b is the diameter of the effective sphere, or the distance between the centers of the contiguous beads, and δ is the $N_b \times (N_b + 1)$ finite difference matrix, which, for the example of $N_b = 3$, is

$$\delta = \begin{pmatrix} -1 & 1 & 0 & 0 \\ 0 & -1 & 1 & 0 \\ 0 & 0 & -1 & 1 \end{pmatrix}. \tag{A10}$$

The potential energy in the y direction for this multiple-bead bending case may be written in terms of the displacement coordinates,

$$U_\eta = \frac{1}{2}\kappa\vec{\eta}^tA\vec{\eta} = \frac{1}{2}\frac{\kappa}{h_b^2}\vec{y}^t\delta^tA\delta\vec{y}. \tag{A11}$$

The force associated with the above potential is

$$\vec{F}(y) = -\frac{\mathrm{d}U}{\mathrm{d}\vec{y}} = -\frac{\kappa}{h_b^2}\delta^tA\delta\vec{y}, \tag{A12}$$

and the associated Langevin equation that contains both the hydrodynamics and the bending is

$$J\ddot{\vec{y}} + \gamma_b\dot{\vec{y}} + \frac{\kappa}{h_b^2}H\delta^tA\delta\vec{y} = \vec{R}(t). \tag{A13}$$

H is the hydrodynamic or the Rotne–Prager-modified-Oseen tensor. The matrix $H\delta^tA\delta$ is diagonalized by a similarity transformation,

$$Q_b^{-1}H\delta^tA\delta Q_b = \Lambda_b, \tag{A14}$$

where Q_b is the transformation matrix and Λ_b is diagonal and contains the $N_b + 1$ eigenvalues. The two lowest eigenvalues of this matrix are zero, and correspond to the translation and rotation (or shear) modes of motion, respectively. These two modes are removed from Λ_b and Q_b when considering the internal dynamics, hence Λ_b is $(N_b - 1) \times (N_b - 1)$ and Q_b is $(N_b + 1) \times (N_b - 1)$. By analogy with Eq. A9, we obtain

$$\langle(\vec{\eta}(t) - \vec{\eta}(0))(\vec{\eta}(t) - \vec{\eta}(0))^t\rangle = 2\frac{k_BT}{\kappa_b}(\delta Q_b)\Lambda_b^{-1}\left(1 - \exp\left\{-\frac{\kappa_b}{h_b^2\gamma_b}\Lambda_bt\right\}\right)(\delta Q_b)^t. \tag{A15}$$

The relaxation time for the lth internal, normal mode (either in terms of displacements or angles) is then

$$\tau_{(\mathrm{bend})_l} = \gamma_bh_b^2/\kappa_b\lambda_{bl}, \tag{A16}$$

where λ_{bl} is the lth eigenvalue in the matrix Λ_b.

The proper choice of bead size, h_b, has been determined (Song et al., 1990); the hydrodynamic interactions are only known for spherical beads, so a section of cylindrical DNA must be substituted by an equivalent sphere. It has been shown that the optimum bead size has radius 15.9 Å or $h_b = 31.8$ Å, which encompasses 9.3 base pairs at 3.4 Å per base pair. This bead size was chosen to ensure that the relaxation times for the effective DNA model reproduce the translational and rotational dynamics for the uniform modes of the rigid object (which is a right circular cylinder). The number of spheres is adjusted so that the total length of the DNA, $h(N + 1) = h_b(N_b + 1)$, is maintained, subject to the constraint that N_b must be an integer. This model is valid for the normal modes in an average sense—the modes represent the $(N_b - 1)$ longest modes from a higher resolution model using the base pair as the fundamental hydrodynamic unit. The translational friction factor, $\gamma_b = 3\pi\eta h_b$, which is needed to obtain the relaxation times for the internal modes for a bead, is related to

the rotational friction factor, $\gamma_{rb} = \pi\eta h_b^3$, by $3\gamma_{rb} = \gamma_b h_b^2$. Regardless of the bead size, the true persistence length must be held unchanged, and so the force constant must be scaled with the bead size $\kappa h = \kappa_b h_b$ (see Eq. 5).

The relaxation times of the internal modes scale according to the ratio of the diameters of the beads. Let $s = h_b/h$ be the scale factor ratio between the two models. The eigenvalues, and hence the relaxation times of the $N_b - 1$ longest modes, can be calculated exactly from the model of Eq. A15, regardless of the scale or bead size. Numerical calculations (not shown) demonstrate that, when the hydrodynamics are neglected $\lambda_{bl}^{-1}(N) = s^4\lambda_{bl}^{-1}(N_b)$ for $3 \le l \le (N_b + 1)$ where $(N + 1) = s \cdot (N_b + 1)$. This relation and Eq. A16 can be used together to show that the relaxation times, $\tau_{(bend)_l}$, are invariant to the scale, s. When hydrodynamics are included, the scaling identity in the above relation is nearly preserved. The term in s^4 is replaced by $s^{3.67}$: $\lambda_{bl}^{-1}(N) = s^{3.67}\lambda_{bl}^{-1}(N_b)$. The scaled bead model (Eq. A16) gives the $(N_b - 1)$ longest relaxation times of the original $(N + 1)$ problem, for any scale factor, s, consistent with the above constraints. DNA with $N + 1$ base pairs should have $N - 1$ internal modes. The mesoscopic model (Schurr et al., 1992) gives the N_b longest modes. N_b is approximately $\frac{1}{10}N$ because the mesoscopic bead size encompasses 9.3 bases in an effective bead and is therefore $9.3 \times 3.4 = 31.8$ Å in diameter. $\tau_{(bead)_l}$ based on a 3.4-Å-diameter bead size admits $N - 1$ modes.

The correlation times may then be written in terms of $h = 3.4$ Å, the diameter of an effective bead. Using Eq. A16 and the scaling relations, the relaxation times for the internal bending modes can be written as

$$\tau_{(bend)_l} = \frac{3\pi\eta h_b^4}{\kappa h \lambda_{bl}(N_b)} = \tau_o \frac{h}{P_{db}\lambda_{bl}(N)} \quad \text{where} \quad \tau_o = s^{0.33}\frac{3\pi\eta h^3}{k_B T}. \tag{A17}$$

For this particular case, $s^{0.33} = 2.11$. τ_o is proportional to the rotational correlation time of a sphere with diameter h, which is $(4\pi\eta(h/2)^3/3k_BT)$. τ_0 is calculated to be 2.2×10^{-10} sec at $T = 0$°C. Eq. A17 is used to calculate $\tau_{(bend)_l}$ for all N internal normal modes, and guarantees that the N_b longest modes are identical to those of the original mesoscopic model. Computation of the internal relaxation times, when taking into account the scaling, is equivalent to multiplying all $\tau_{(bend)_l}$ by 2.11 from a calculation which neglects the scaling.

We now develop how to calculate the transformation matrix, Q_b. The equilibrium mean squared amplitudes of oscillation for the flexural motion, given in Eq. A15, relies on the matrix Q_b: the similarity transformation matrix defined by the Langevin equation containing both hydrodynamic and bending forces (Eq. A13). H, as given by Song et al. (1990), is a symmetric Toeplitz matrix (MathWorks, 1996) formed from the column vector $C = (1\ c_1\ \cdots\ c_{N_b})^t$, where the elements are defined as

$$c_m = \frac{3}{8m}\left\{1 + \frac{1}{6m^2}\right\}.$$

Because of this form, H is symmetric, and all of the eigenvalues of H are positive. The Langevin Eq. A13 can be separated into a set of normal mode equations by the similarity transformation, $Q_b^{-1}H\delta^t A\delta Q_b = \Lambda_b$, and in terms of the normal modes, $y = Q_b\rho$. Each internal normal mode equation can be solved independently. Most modern eigenvalue packages (MathWorks, 1996) will return a set of eigenvectors that will properly diagonalize the $H\delta^t A\delta^t$ matrix. However, to insure that the internal potentials remain invariant to the transformation,

$$U_\eta = \frac{1}{2}\frac{\kappa_b}{h_b^2}\vec{y}^t\delta^t A\delta\vec{y} = \frac{1}{2}\frac{\kappa_b}{h_b^2}\vec{\rho}^t Q_b^t\delta^t A\delta Q_b\vec{\rho} = \frac{1}{2}\frac{\kappa_b}{h_b^2}\vec{\rho}^t\Lambda\vec{\rho} \tag{A18}$$

The matrix Q_b must perform a congruent transformation on the matrix $D = \delta^t A\delta$, as well as a similarity transformation of the matrix HD. We will show by construction of Q_b that this is one of the properties of Q_b. The two uniform modes do not contribute to the total potential U_η because they have zero eigenvalues; and this must be the case on physical grounds, because U_η is an internal potential.

We follow the previous treatment (Song et al., 1990) with the following variation: Because the matrix H is symmetric, it can be diagonalized by a real orthogonal transformation,

$$T^t H T = \mu. \tag{A19}$$

From this, one can define $H^{1/2} = T\mu^{1/2}T^t$, moreover $H^{-1/2}$ is well defined because H is not singular (a property that D does not share). It follows that

$$H^{1/2}DH^{1/2}H^{-1/2}Q_b = H^{-1/2}Q_b\Lambda_b. \tag{A20}$$

Because $H^{1/2}DH^{1/2}$ is symmetric, it can be diagonalized by an orthogonal transformation U, and must have the same eigenvalues as the original problem,

$$U^t(H^{1/2}DH^{1/2})U = \Lambda_b. \tag{A21}$$

Consequently, the matrix Q_b is related to U by

$$Q_b = H^{1/2}U. \tag{A22}$$

By this prescription then, we generate a Q_b, which has the following properties:

$$Q_b^t D Q_b = (H^{1/2}U)^t D(H^{1/2}U) = \Lambda_b$$

and

$$Q_b^{-1}H(Q_b^{-1})^t = (H^{1/2}U)^{-1}H((H^{1/2}U)^{-1})^t = 1. \tag{A23}$$

This is a minor variation on the development of Schurr, but it is more straightforward in that all the eigenvalues of H are positive and the r.h.s. of Eq. A15 is of the same form as Eq. A9. This Q_b is related to the one defined by Schurr, Q_s, by $Q_b \cdot \Lambda^{-1/2} = Q_s$ for the nonzero eigenvalue vectors, and the first two vectors of Q_s are identical to the first two vectors of Q_b, which have eigenvalues of zero.

It is not at all obvious that Eq. A9 leads to exactly the same results as Eq. A4b in the infinite-time limit, because neither the set of eigenvalues nor the transformation matrix is the same as the analogous quantities of Eq. A4b. The mean square displacements are identical however, when the transformation matrix Q_b is suitably modified. One requirement of the solutions is that, at infinite time, the mean squared angular displacements with respect to the end-to-end vector must be the same as given directly from the matrix **A**, as shown in Eqs. A3 and A4. Therefore, we require that

$$\delta Q_b\Lambda_b^{-1}(\delta Q_b)^t = A^{-1}, \tag{A24}$$

where A^{-1} implies the pseudo or generalized inverse of **A**, (MathWorks, 1996).

The eigenvectors Q_b, computed according to the above prescription, or by using Eq. 79 of the previous development (Song et al., 1990), do not immediately satisfy this requirement, because the odd eigenvectors are mixed with some of the rotation from the uniform rotational vector (the second eigenvector of Q_b). Note that the third mode of Q_b is always even, when the eigenvalues Λ_b are in ascending order. The rotational (shear mode) contamination in the odd modes of Q_b is removed by rotating the displacements until the base pairs on either end of the rod are zero. All of the odd modes contained in Q_b are the even numbered vectors. Specifically, the even vectors of Q_b ($k = 4, 6, 8, \ldots, N + 1$), are modified for all values of j, $1 \le j \le N_b + 1$, and replaced by the following prescription:

$$(\tilde{Q}_b)_{j,k} = (Q_b)_{j,k} - (Q_b)_{j,2} \cdot \frac{(Q_b)_{1,k}}{(Q_b)_{1,2}}. \tag{A25}$$

This method of calculation provides us with a set of eigenvalues and eigenvectors that are used to obtain the mean square oscillation amplitudes (Eq. A15) and decay times for each of the modes (Eq. 7). The modification in Eq. A25 of the transformation matrix Q_b is essential to ensure that the

results obtained using Eq. A15 are identical to those of Eqs. 3 and A4. The $\tilde{Q}_b$ so rotated, (Eq. A25), no longer diagonalizes the *HD* matrix, but it does give the same answers at infinite time as the *Q* matrix, which diagonalized **A**, Eqs. A3, and A4. Therefore, we use the $\tilde{Q}_b$ matrix.

This work was supported in part by grants from the National Institute of Health (GM 32681 and GM 08268 (A.W.R.)) and National Institute of Environmental Health Sciences Environmental Sciences Center Grant P30 ESO7033, as well as a fellowship from the American Chemical Society (S.C.A.). Thanks to Mickey Schurr and Eric Hustedt for many helpful discussions and insights, and Dr. A. Smirnov of the Illinois EPR Research Center (IERC) facility at the University of Illinois.

REFERENCES

Alam, T. M., and G. P. Drobny. 1991. Solid-state NMR studies of DNA structure and dynamics. *Chem. Rev.* 91:1545–1590.

Allison, S. A., R. Austin, and M. Hogan. 1989. Bending and twisting dynamics of short linear DNAs. Analysis of the triple anisotropy decay of a 209 base pair fragment by Brownian simulations. *J. Chem. Phys.* 90:3843–3854.

Alley, S. C. 1996. The sequence-dependence of DNA flexibility. Ph.D. thesis, University of Washington, Seattle, WA.

Barkley, M. D., and B. H. Zimm. 1979. Theory of twisting and bending of chain macromolecules: analysis of the fluorescence depolarization of DNA. *J. Chem. Phys.* 70:2991–3007.

Eimer, W., J. R. Williamson, S. G. Boxer, and R. Pecora. 1990. Characterization of the overall and internal dynamics of short oligonucleotides by depolarized dynamic light scattering and NMR relaxation measurements. *Biochemistry.* 29:799–811.

Forster, D. 1975. Hydrodynamic Fluctuations, Broken Symmetry, and Correlation Functions. Benjamin, New York, NY.

Freed, J. H. 1976. Theory of slow tumbling ESR spectra for nitroxides. *In* Spin Labeling: Theory and Applications, L. J. Berliner, editor. Academic Press, New York. 53–132.

Goldstein, A. 1975. Classical Mechanics. Addison-Wesley, New York, NY. 104.

Griffith, O. H., and P. Jost. 1976. Lipid spin labels in biological membranes. *In* Spin Labeling: Theory and Applications, L. J. Berliner, editor. Academic Press, New York. 454–523.

Hagerman, P. J. 1988. Flexibility of DNA. *In* Annual Reviews of Biophysics and Biophysical Chemistry, D. M. Engelman, C. E. Cantor, and T. D. Pollard, editors. Annual Reviews, Palo Alto, Ca. 17:265–285.

Hogan, M. E., and O. Jardetzky. 1979. Internal motions in DNA. *Proc. Natl. Acad. Sci. USA.* 76:6341–6345.

Hogan, M. E., and O. Jardetzky. 1980. Internal motions in deoxyribonucleic acid II. *Biochemistry.* 19:3460–3468.

Hustedt, E. J., J. J. Kirchner, A. Spaltenstein, P. B. Hopkins, and B. H. Robinson. 1995. Monitoring DNA dynamics using spin labels with different independent mobilities. *Biochemistry.* 34:4369–4375.

Hustedt, E. J., A. Spaltenstein, J. J. Kirchner, P. B. Hopkins, and B. H. Robinson. 1993a. Motions of short DNA duplexes: an analysis of DNA dynamics using an EPR-active probe. *Biochemistry.* 32:1774–1787.

Hustedt, E. J., C. E. Cobb, A. H. Beth, and J. M. Beecham. 1993b. Measurement of rotational dynamics by the simultaneous non-linear analysis of optical and EPR Data. *Biophys. J.* 64:614–621.

Keyes, R. S., and A. M. Bobst. 1995. Detection of Internal and Overall Dynamics of a Two-Atom-Tethered Spin-labeled DNA. *Biochemistry.* 34:9265–9276.

Lipari, G., and A. Szabo. 1981. Nuclear magnetic resonance relaxation in nucleic acid fragments: models for internal motion. *Biochemistry.* 20: 6250–6256.

Lipari, G., and A. Szabo. 1982a. Model-free approach to the interpretation of nuclear magnetic resonance relaxation in macromolecules. 1. Theory and range of validity. *J. Am. Chem. Soc.* 104:4546–4559.

Lipari, G., and A. Szabo. 1982b. Model-free approach to the interpretation of nuclear magnetic resonance relaxation in macromolecules. 2. Analysis of experimental results. *J. Am. Chem. Soc.* 104:4559–4570.

Mailer, C., S. J. Danielson, and B. H. Robinson. 1985. Computer-controlled pulsed-EPR spectrometer. *Rev. Sci. Instrum.* 56:1917–1930.

Mailer, C., D. A. Haas, E. J. Hustedt, J. G. Gladden, and B. H. Robinson. 1991. Low-power electron paramagnetic resonance spin-echo spectroscopy. *J. Magn. Reson.* 91:475–496.

MathWorks, I. 1996. Using MATLAB: The Language of Technical Computing. MathWorks Inc., Natick, MA. 4–22.

Mattiello, D. L., and G. P. Drobny. 1994. Investigating furanose ring dynamics in oligonucleotides with solid state 2H NMR. *In* NMR Probes of Molecular Dynamics, R. Tycko, editor. Kluwer Academic Press, Amsterdam, The Netherlands. 335–372.

Miller, T. R., S. C. Alley, A. W. Reese, M. S. Solomon, W. V. McCallister, C. Mailer, B. H. Robinson, and P. B. Hopkins. 1995. A probe for sequence-dependent nucleic acid dynamics. *J. Am. Chem. Soc.* 117: 9377–9378.

Nordio, P. L. 1976. General magnetic resonance theory. *In* Spin Labeling: Theory and Applications, L. J. Berliner, editor. Academic Press, New York. 5–52.

Nuutero, S., B. S. Fujimoto, P. F. Flynn, B. R. Reid, N. S. Ribeiro, and J. M. Schurr. 1994. The amplitude of local angular motion of purines in DNA in solution. *Biopolymers.* 34:463–480.

Okonogi, T. M., A. W. Reese, S. C. Alley, P. B. Hopkins, and B. H. Robinson. 1997. Sequence dependent dynamics of duplex DNA. Paper presented at the 20th International EPR Conference: 39th Rocky Mountain Conference, Aug. 3–7, Denver, CO.

Reese, A. W. 1996. Analysis of CW-EPR spectra and the internal dynamics of DNA. Ph.D. thesis, University of Washington, Seattle, WA.

Reese, A. W., S. C. Alley, T. R. Miller, P. B. Hopkins, and B. H. Robinson. 1996a. Length and probe position dependence of DNA dynamics. Paper presented at the XVII International Conference on Magnetic Resonance in Biological Systems, Aug. 18–23, Keystone, CO.

Reese, A. W., S. C. Alley, T. R. Miller, P. B. Hopkins, and B. H. Robinson. 1996b. Sequence Dependence of DNA Dynamics. Paper presented at the XVII International Conference on Magnetic Resonance in Biological Systems, Aug. 18–23, Keystone, Co.

Robinson, B. H., and G. P. Drobny. 1995a. Site specific dynamics in DNA: theory. *In* Annual Reviews of Biophysics and Biomolecular Structure, R. M. Stroud, W. L. Hubbell, and W. K. Olson, editors. Annual Reviews Inc., Palo Alto, CA. 24:523–549.

Robinson, B. H., and G. P. Drobny. 1995b. Site-specific dynamics in DNA: theory and experiment. *In* Methods in Enzymology, T. L. James, editor. Academic Press, San Diego, CA. 261:451–509.

Robinson, B. H., G. Forgacs, L. R. Dalton, and H. L. Frisch. 1980. A simple model for internal motion of DNA based upon EPR studies in the slow motion region. *J. Chem. Phys.* 73:4688–4692.

Robinson, B. H., C. Mailer, and G. P. Drobny. 1997. Site specific dynamics in DNA: experiments. *In* Annual Reviews of Biophysics and Biomolecular Structure, R. M. Stroud, W. L. Hubbell, and W. K. Olson, editors. Annual Reviews Inc., Palo Alto, CA. 26:629–658.

Schellman, J. A., and C. H. Harvey. 1995. Static contributions to the persistence length of DNA and dynamic contributions to DNA curvature. *Biophys. Chem.* 55:95–114.

Schurr, J. M. 1976. Relaxation times manifested by the Rouse–Zimm model in dynamic light scattering experiments. *Biopolymers.* 16: 461–464.

Schurr, J. M., B. S. Fujimoto, P. Wu, and L. Song. 1992. Fluorescence studies of nucleic acids: dynamics, rigidities, and structures. *In* Topics in Fluorescence Spectroscopy, J. R. Lakowicz, editor. Plenum Press, New York. 137–229.

Schurr, J. M., H. P. Babcock, and B. S. Fujimoto. 1994. A test of the model-free formula. Effects of anisotropic and rotational diffusion and dimerization. *J. Mag. Res. B.* 105:211–224.

Schurr, J. M., B. Fujimoto, and B. H. Robinson. 1997. Diffusional spinning as a probe of DNA fragments conformation—comment. *J. Chem. Phys.* 106:815–816.

Shibata, J. H., B. S. Fujimoto, and J. M. Schurr. 1985. Rotational dynamics of DNA from 10(−10) to 10(−5) seconds: comparison of theory with optical experiments. *Biopolymers.* 24:1909–1930.

Song, L., S. A. Allison, and J. M. Schurr. 1990. Normal mode theory for Brownian dynamics of a weakly bending rod: comparison with Brownian dynamics simulations. *Biopolymers.* 29:1773–1791.

Strobel, O. K., R. S. Keyes, R. R. Sinden, and A. M. Bobst. 1995. Rigidity of a B-Z region incorporated into a plasmid as measured by electron paramagnetic resonance. *Biochemistry.* 324:357–366.

Thomas, D. D., J. C. Seidel, J. Gergely, and J. S. Hyde. 1975. The quantitative measurement of rotational motion of the subfragment-1 region of myosin by saturation transfer EPR spectroscopy. *J. Supramol. Struct.* 3:376–390.

Tirado, M. M., and J. Garcia de la Torre. 1980. Rotational dynamics of a rigid symmetric top macromolecule application to circular cylinders. *J. Chem. Phys.* 73:1986–1993.

Trifonov, E. N., R. K.-Z. Tan, and S. C. Harvely. 1987. Static and dynamic components of the persistence length of DNA. *In* DNA Bending and Curvature, W. K. Olson, M. H. Sarma, and M. Sundaralingam, editors. Adenine Press, New York.

Van, S. P., G. B. Birrell, and O. H. Griffith. 1974. Rapid anisotropic motion of spin labels: models for motion averaging of the ESR parameters. *J. Magn. Reson.* 15:444–459.

Wilcoxon, J., and J. M. Schurr. 1983. Temperature dependence of the dynamic light scattering of linear phi 29 DNA: implications for spontaneous opening of the double helix. *Biopolymers.* 22:2273–2321.

Wu, P., B. S. Fujimoto, and J. M. Schurr. 1987. Time-resolved FPA of short restriction fragments. The friction factor for rotation of DNA about its symmetry axis. *Biopolymers.* 26:1463–1488.